NACA RM L57K27

NACA

RESEARCH MEMORANDUM

TRANSONIC INVESTIGATION OF AN AXIAL-FLOW COMPRESSOR ROTOR WITH A CONTRACTED EXIT ANNULUS

By Robert S. Babington

Langley Aeronautical Laboratory
Langley Field, Va.

Declassified January 12, 1961

NATIONAL ADVISORY COMMITTEE
FOR AERONAUTICS
WASHINGTON
February 17, 1958

NATIONAL ADVISORY COMMITTEE FOR AERONAUTICS

RESEARCH MEMORANDUM

TRANSONIC INVESTIGATION OF AN AXIAL-FLOW COMPRESSOR ROTOR WITH A CONTRACTED EXIT ANNULUS

By Robert S. Babington

SUMMARY

An axial-flow compressor rotor with a 13-percent reduction in exit annulus was investigated in a medium of Freon-12 gas at air equivalent tip speeds ranging from 808 to 1,244 feet per second. The blade sections employed were cambered in accordance with the NACA A_2I_{8b} mean-line series.

The overall design total-pressure ratio was attained at a mean section angle of attack 4.5° greater than the low-speed design value taken from two-dimensional cascade data. The minimum values of total-pressure-loss coefficient increased rapidly when the inlet relative Mach numbers exceeded 0.95.

In order to analyze the results caused by the reduction in exit annulus, the performance of the rotor was compared with that of the same rotor with a constant annular area. It was found that the reduction in exit annulus increased the operating range of the compressor and reduced the diffusion. Throughout most of the range of operation, the reduction in exit annulus also effected an increase in the overall rotor efficiency.

INTRODUCTION

In the design of axial-flow compressors for turbojet engines, it has always been desirable to obtain high specific weight flow, high pressure ratio per stage, and high efficiency. To obtain these characteristics, the axial velocity and rotational speed were increased until transonic inlet relative Mach numbers were reached (approximately 1.1 at the rotor tip). In order to accommodate these high Mach numbers without excessive losses, the mean-line blade-element shape was altered to shift the loading rearward where the blade-surface Mach numbers were lower (ref. 1).

The rotor reported in references 2 and 3 employs blades that contain loaded trailing-edge mean lines, but the diffusion required at the tip section of the rotor was large. It was believed that a reduction in exit annular area would reduce the high diffusion that was required and, accordingly, increase the rotor efficiency. Consequently, the rotor of references 2 and 3 was modified to include a 0.3-inch hub buildup which constituted a 13-percent decrease in exit annular area.

This report presents both an overall and a blade-element analysis of the modified rotor and compares the results with those obtained from the rotor of references 2 and 3 (no hub buildup).

SYMBOLS

c	blade chord, ft
c_p	specific heat at constant pressure, $\frac{\text{ft-lb}}{\text{slugs-}^{\circ}\text{F}}$
C_p	static-pressure-rise coefficient, $\frac{p_2 - p_1}{P_{1,R} - p_1}$
D	diffusion factor, $1 - \frac{V_{2,R}}{V_{1,R}} + \frac{\Delta V_\theta}{2\sigma V_{1,R}}$
g	acceleration due to gravity, 32.2 ft/sec^2
M	Mach number
n	rotor speed, rps
p	static pressure, lb/sq ft
P	total pressure, lb/sq ft
r	radius, ft
R	universal gas constant
T	total temperature, $^{\circ}$R
U	blade tangential speed, $2\pi nr$, ft/sec

V velocity, ft/sec

w gas weight flow, lb/sec

$\frac{w\sqrt{\theta}}{\delta}$ equivalent weight flow corrected to sea-level conditions, lb/sec

α angle of attack, angle between flow direction and blade chord, deg

β gas flow angle, based on flow direction with respect to axial direction, deg

γ ratio of specific heats

δ ratio of inlet total pressure at test conditions to standard sea-level pressure, $\frac{P_1}{2116}$

Δ increase from station 1 to station 2

η momentum efficiency

θ ratio of inlet total temperature at test conditions to standard sea-level total temperature, $\frac{T_1}{518.6}$

θ_o rotor turning angle, deg

ρ gas density, slugs/cu ft

σ solidity

$\bar{\omega}$ relative total-pressure-loss coefficient, $\frac{P_{1,R} - P_{2,R}}{P_{1,R} - p_{1,R}}$

Subscripts:

av average

d design

max maximum

min minimum

R	rotor blade
t	tip
z	axial
θ	tangential
1	upstream of rotor
2	downstream of rotor

A bar over a symbol indicates mass-flow weighted average.

APPARATUS AND METHODS

Rotor Design

The axial-flow compressor rotor used in this investigation is pictured in figure 1. A drawing of the hub contour and the assumed streamline paths near the hub, mean, and tip sections is shown in figure 2. The original rotor was 16 inches in diameter and was designed to operate at a weight flow in air of 19.99 pounds per second (37.00 pounds per second in Freon-12), a tip speed of 808 feet per second, an efficiency of 92 percent, and a total-pressure ratio of 1.258. The design velocity diagrams for the rotor without the reduction in exit annulus were taken from reference 2 and are presented in figure 3 for the hub, mean, and tip sections. The blade sections were cambered in accordance with the NACA A_2I_{8b} mean-line series for isolated lift coefficients of 1.85, 1.13, and 0.73 at the hub, mean, and tip, respectively. Blade thickness varied from 10 percent of the chord at the hub to 8 percent of the chord at the tip, while the solidity remained constant at 1.0. The inlet hub-tip ratio was 0.750 and the hub buildup produced an outlet hub-tip ratio of 0.788. Other design characteristics of lesser importance are listed in table form in reference 2.

Instrumentation

A prism probe (ref. 4) was used downstream of the rotor to measure total pressure, static pressure, and turning angles at 11 stations across the annulus area. The spacing of the stations was closest at the walls because at these locations there is generally more variation in the flow characteristics.

Two four-element thermocouple rakes were installed downstream of the rotor so that the eight elements adequately covered the annulus. A four-element thermocouple was installed upstream and connected to the two downstream thermocouples in such a way that the change in temperature across the rotor could be measured directly.

Four iron-constantan thermocouples and four L-shaped total-pressure tubes were mounted in the settling chamber to record inlet stagnation temperature and pressure. Static-pressure orifices were utilized to measure upstream and downstream static pressures at the walls and were equally spaced circumferentially. The downstream orifices were located in the same plane as the survey instrument. The methods used to determine motor speed, motor torque, and Freon purity are identical with those used in references 2 and 3.

Test Procedure

The rotor was tested at speeds of n/n_d = 1.00, 1.18, 1.37, 1.45, and 1.54 corresponding to air equivalent tip speeds of 808 to 1,244 feet per second. The weight-flow range was varied from maximum weight flow (determined by the limitations of the rig) to a point very close to surge with data taken at a total of five throttle settings. The tests were performed in a medium of Freon-12 gas, and a schematic drawing of the test rig used is shown in figure 4.

Data Reduction

In order to tabulate the data on an equal-area basis, the inlet and outlet were divided into 10 annuli of equal areas. Test values for the centers of the 10 annuli were obtained from a curve connecting the measured values taken at the 11 survey stations. The downstream variation in static pressure was determined by fairing a curve between the wall static-pressure values and the static-pressure values obtained from the survey instrument, while the upstream static-pressure variation was considered to be linear. The values of inlet and outlet weight flow were determined by integrating the product of local density and axial velocity. The upstream weight-flow values were considered more reliable than those at the outlet because of the steady nature of the flow ahead of the rotor. For this reason, all the performance curves presented are given as a function of inlet weight flow. The equations used to find mass-flow weighted total-pressure ratio and efficiency can be found in reference 2 as well as the conversion formulas for air equivalent rotational speed and weight flow. A derivation, considering the contraction in exit annulus, yielded the following expression from which the relative total-pressure-loss parameters were computed:

[redacted]

$$\bar{\omega} = \frac{\left[1 + \frac{U_{1,t}^{2}\left(\frac{r_2^{2} - r_1^{2}}{r_t^{2}}\right)}{2T_1 c_{p_{av}}}\right]^{\left(\frac{c_p}{R}\right)_{av}} - \frac{P_{2,R}}{P_{1,R}}}{1 - \frac{p_1}{P_{1,R}}}$$

Validity of Data

In order to investigate the continuity of the flow measurements made upstream and downstream, figure 5 was plotted to show a comparison at the two locations. All the values for speeds of $n/n_d = 1.00$, 1.18, and 1.37 were within 2 percent of agreement except for one point at design speed, for which the upstream and downstream measurements differed by 4.3 percent. At the two highest speeds, all the values were within a 3-percent agreement except for two points; one, at a speed of $n/n_d = 1.54$, differed by 4.25 percent and the other, by 3.35 percent near surge at a speed of $n/n_d = 1.45$.

During the test program, there were instances when the blade-element efficiency exceeded 100 percent and the relative loss coefficients fell below zero. In the rotor design, it was assumed that the streamlines would follow conical paths through the centers of the equal area (fig. 2). However, because of variations in losses, power input, and other variables which affect radial equilibrium, the exact path of the streamlines could not be predicted accurately. This fact was probably responsible for the erroneous values in relative loss coefficient. Likewise, the inlet flow was assumed to be uniform, but slight flow irregularities could have caused efficiencies in excess of 100 percent in regions where the rotor was very efficient. However, since these testing conditions existed throughout the entire program, the trends in the performance parameters are accurate even if the levels of the values are slightly in error. With this fact in mind and in view of the relatively close agreement in flow measurement, it is concluded that the available data are reliable enough for a good analysis of the rotor performance.

RESULTS AND DISCUSSION

Overall Performance

The mass-averaged rotor-performance data are plotted in figure 6. Mass-averaged total-pressure ratio and the mass-averaged momentum efficiency were plotted against equivalent Freon weight flow.

At design speed and design weight flow (37.0 pounds per second), the efficiency was 90 percent and the total-pressure ratio was 1.18. The corresponding design values for efficiency and total-pressure ratio were 92 percent and 1.258, respectively. At a weight flow of 32.0 pounds per second, the design pressure ratio was equaled and an efficiency of 97 percent was obtained.

At speeds greater than design, the rotor appeared to be choked in the region of high weight flow. Evidence of this condition is given by the slopes of all the efficiency and pressure-ratio curves as they increase to infinity at maximum weight flow. The peak efficiency remained at 80 percent or higher throughout the speed range and the highest total-pressure ratio observed was 1.63 at a speed of $n/n_d = 1.54$.

Radial Variation of Performance

Because of the three-dimensional effects that occur in a rotating compressor, it is necessary to analyze its radial variation of performance. The characteristics presented are momentum efficiency η, inlet relative Mach number $M_{1,R}$, elemental weight flow leaving the rotor $g\rho_2 V_{z,2}$, exit absolute Mach number M_2, inlet relative air angle $\beta_{1,R}$, and total-pressure ratio P_2/P_1. (In order to facilitate presentation of the data, staggered scales have been used in the performance-characteristic figures and care should be taken in identifying the proper scale for each curve.)

Figure 7 shows that the efficiency at design speed remained high throughout a large portion of the blade radius, but the radial extent of high efficiency diminished as the speed was increased. At the top speed of $n/n_d = 1.54$, the only highly efficient portion of the blade was near the hub. At all speeds as the weight flow increased, the efficiency decreased and the rate of decrease was greatest at the hub and tip. At maximum weight flow, the efficiency underwent a decrease along the entire blade height, especially at the higher speeds.

Figure 8 presents the variation of inlet relative Mach number as a function of radius. The Mach numbers increased linearly from hub to tip and ranged from 0.64 at design speed to 1.27 at a speed of $n/n_d = 1.54$. As a result of the high inlet relative Mach numbers at the tip, the centrifuging of boundary layer (ref. 5), and the secondary flow at the casing, separation occurred at the rotor tip first. A flow shift towards the hub accompanied the separation and evidence of this is shown in figure 9 by the radial variation of weight flow leaving the rotor. At the lower speeds, as would be expected in a free vortex design, the weight flow was uniform across the exit annulus except near the extreme hub and tip; but, as the speed was increased, the hub section was seen to pass most of the flow. The radial variation of exit absolute Mach number shown in figure 10 also supports this conclusion; that is, with speed increase the exit absolute Mach numbers at the hub became greater than those at the tip.

The radial variation of inlet relative air angle is shown in figure 11 along with the design values taken from the velocity diagrams of figure 3. It can be seen that the slopes of the measured values of $\beta_{1,R}$ are very similar to that of the design curve. This would, therefore, validate the original assumption of constant inlet axial velocity.

The radial variation of total-pressure ratio is presented in figure 12. At speeds of $n/n_d = 1.00$ and 1.18, the pressure ratio remained constant from hub to tip, but, as the speed increased, the pressure ratio at the hub was slightly greater than that at the tip and mean sections.

Blade-Element Performance

The blade-element characteristics are plotted against angle of attack in figures 13, 14, and 15. The three elements that were analyzed are located by dashed lines in figure 2. Because of secondary flow that occurs in compressors in the regions adjacent to the inner and outer casings, it was felt that the data at points 1 and 10 would not be indicative of the blade performance. Points 2, 6, and 9 were chosen to represent the tip, mean, and hub sections, respectively. The performance parameters presented are section efficiency η, relative total-pressure-loss coefficient $\bar{\omega}$, inlet relative Mach number $M_{1,R}$, static-pressure-rise coefficient C_p, diffusion factor D, total-pressure ratio $\frac{P_2}{P_1}$, static-pressure ratio $\frac{p_2}{p_1}$, turning angle θ_o, and axial velocity ratio $\frac{V_{z,2}}{V_{z,1}}$. The original rotor design angles of attack taken from the difference between relative inlet air angles $\beta_{1,R}$ of figure 3 and the blade-setting angles $\beta_{1,R} - \alpha$ have been noted on the plots as vertical arrows on the abscissa.

Mean section.- Figure 13 presents the mean-section performance plots. At design speed and 118 percent of design speed, the efficiency was fairly constant throughout the angle-of-attack range, and for the most part was higher than 95 percent. As the speed increased from $n/n_d = 1.37$ to $n/n_d = 1.54$, the efficiency as a whole grew progressively worse with a sharp dip occurring at the maximum weight flow for each speed. At design speed and design angle of attack, the efficiency was 98.5 percent. Design angle of attack was 9.4° for the mean section. At all radial locations, the entire operating range of the compressor was above design angle of attack with the exception of the maximum weight-flow condition at design speed. The trends of the efficiency curves support the conclusions made in the reports of other transonic rotors, for example, reference 6, in that rotors operated more efficiently at angles of attack greater than the design values based on low-speed two-dimensional cascade data.

The losses encountered at design speed and 118 percent of design speed were very small for the greater portion of the angle-of-attack range, with a slight rise occurring at maximum weight flow. At the higher speeds, the minimum total-pressure-loss coefficient reached a level of about 0.20 at a speed of $n/n_d = 1.54$ and an angle of attack of 15°. The inlet relative Mach number at this point was 1.14.

A measure of blade loading is presented in the plots of static-pressure-rise coefficient and diffusion factor. Both parameters reached a maximum at a speed of $n/n_d = 1.18$ and began to drop off as the speed was increased. This indicates that the blade section was overloaded at speeds of $n/n_d = 1.37$, 1.45, and 1.54. It should be noted that the overloaded condition occurred as soon as the inlet relative Mach numbers approached unity.

The total- and static-pressure-ratio curves exhibit the same trends with the total-pressure values being somewhat higher. The choking condition that was mentioned briefly in the section entitled "Overall Performance" is evident in the pressure-ratio curves. At maximum weight flow for speeds of $n/n_d = 1.37$, 1.45, and 1.54, the curves exhibit a rapid drop in pressure ratio, indicating that the rotor was choked at these conditions. As the back pressure was increased (angle of attack increased), the choking was relieved as the shock wave steepened and moved upstream. The shadowgraphs in reference 6 illustrate this point. At maximum angle of attack, the same peak static-pressure ratio (about 1.35) was realized for speeds of $n/n_d = 1.37$, 1.45, and 1.54. In order to obtain the design total-pressure ratio of 1.258, the blade element had to operate at an angle of attack of 13.8° or about 4° above design.

The variation of turning angle with angle of attack, taken from the low-speed cascade data of reference 1, is included in figure 13 and the

data show that the design flow turning of 14.5° was accomplished at design angle of attack. Good agreement occurred between the cascade turning and the turning produced by the subject rotor at design speed and 118 percent of design speed at the lower angles of attack. However, at the higher speeds, there was considerable variation and the divergence indicates that low-speed cascade data must be corrected to predict accurately high-speed rotor turning.

Tip section.- The tip-section performance characteristics are shown in figure 14. At design speed, the tip-section efficiency reached a maximum of 86 percent at an angle of attack of 11° (approximately 3° above design). As the angle of attack was increased, the tip losses began to rise and the efficiency dropped to 76 percent at an angle of attack of 15.5°. As a comparison, the mean section, because of its wider low-loss operating range, was seen to have relatively constant efficiency throughout the entire angle-of-attack range at this speed.

The inlet relative Mach numbers for speeds of $n/n_d = 1.00$ and 1.18 never exceeded 1.0. In general, the parameters of these two speeds exhibited the same trends and are discussed simultaneously. A similar grouping occurred for the curves at speeds of $n/n_d = 1.37$, 1.45, and 1.54 where the inlet relative Mach numbers were above 1.0. The distinction between the two groups occurs because of shock-wave effects.

Contrary to what might be expected, the regions of highest relative total-pressure-loss coefficient exhibit the highest efficiencies at high speed. Apparently, the rapid rise in pressure ratio more than compensated for the effects of the rise in relative loss coefficient.

A low-speed cascade turning curve was again superimposed on the plot of rotor turning angle and angle of attack, and good agreement was shown at speeds of $n/n_d = 1.00$ and 1.18. The design turning angle was approximately 10.0° and was closely approached as the tip section actually turned the flow 11.2° at design speed and design angle of attack. At the higher speeds of $n/n_d = 1.37$, 1.45, and 1.54, the turning angle varied from -2° to 11° in an angle-of-attack range from 11.4° to 16.1°. The turning angle at speeds of $n/n_d = 1.37$ and 1.45 reached a minimum in the middle of the angle-of-attack range and then began to rise again at higher angles of attack. The location of the shock wave on the blade was probably responsible for this phenomenon. As the weight flow decreased, the shock was moved upstream where its strength on the convex surface of the blade was less. This action lessened the tendency for flow separation and increased the turning angle.

The variation of static-pressure ratio with angle of attack presents an interesting point that was also observed at the mean section. At

maximum angle of attack for speeds of $n/n_d = 1.37$, 1.45, and 1.54, the values of static-pressure ratio grouped together at a peak value of about 1.37. The value noted at the mean section was about 1.35.

Reference 7 gives a value of 0.45 as the low-loss limiting diffusion factor for the tip section. This value was obtained from the correlation of data, based on minimum loss conditions. At the design speed for this rotor, the tip losses start to rise at a diffusion factor of about 0.48 and at a corresponding angle of attack about 2° above design.

Hub section.- Figure 15 shows that the losses at the hub section were relatively low with only four points having a total-pressure-loss coefficient greater than 0.1. These four values were the maximum flow points at the four highest speeds where the passage was choked. At the other end of the angle-of-attack range (near stall), the losses at the hub did not rise as did those at the mean and tip sections, and this could be due to the radial flow shift towards the hub or the centrifuging of boundary layer.

At the tip section, the axial-velocity ratio decreased as the angle of attack increased, the drop being especially rapid at the higher speeds where the flow separation was more severe. At the hub section, the axial-velocity ratio increased with angle of attack, this increase indicating a flow shift towards the hub. The axial-velocity ratio at the mean section remained relatively constant, receiving flow from the tip and discharging flow to the hub. The logic just presented is sound for the portion of the curves discussed (high angles of attack). However, it appears somewhat faulty in the regions of low angles of attack because at these points the axial-velocity ratio decreased at all three radial locations. This might be attributed to compressibility effects caused by the increase in back pressure. As the angle of attack was increased, the density increased rapidly at first, causing a decrease in exit velocity all along the blade row. Note that this is true because the exit Mach numbers were subsonic. (See fig. 10.) But with further increase in angle of attack, the differential increase in density became less and, consequently, its effect on velocity ratio became less noticeable.

The relative inlet Mach number range varied from 0.67 at design speed to 1.07 at a speed of $n/n_d = 1.54$. At the hub section, the highest speed is the only one at which supersonic inlet relative Mach numbers existed, but the rapid decrease of the static- and total-pressure-ratio curves indicates that choking occurred near maximum weight flow for all speeds except design. At the hub, the greater blade thickness and smaller inlet angles caused choking to occur at lower inlet relative Mach numbers than at the other blade sections.

It was seen that at high speeds and maximum angle of attack, the static-pressure ratios peaked at 1.35 and 1.37 at the mean and tip sections,

respectively. At the hub section, the same condition occurred with the peak static-pressure ratio reaching a value of about 1.33 at maximum angle of attack for speeds of $n/n_d = 1.37$, 1.45, and 1.54.

At design speed, the design amount of flow turning was accomplished at an angle of attack about 5° greater than design. At design angle of attack, 14.5° of turning was produced in comparison to a design value of approximately 21°.

Relative total-pressure-loss coefficient.- Relative total-pressure-loss coefficient is plotted against diffusion factor and static-pressure-rise coefficient in figure 16 for all speeds at the hub, mean, and tip sections. The curves were faired in a sequence of increasing speed so that the effects of speed on blade loading could be seen to better advantage. The minimum value of relative loss coefficient usually occurs when the efficiency is a maximum, but this was not the case at the tip section of the subject rotor. Therefore, at the tip section, the minimum value of relative loss coefficient as well as the value of relative loss coefficient corresponding to maximum efficiency $\bar{\omega}_{\eta max}$ were plotted for all speeds against each of the two blade-loading parameters.

A tip-section band of low-loss diffusion factors was established in reference 7 from the compiled data of a number of rotors and was reproduced on the tip-section plot of figure 16. For speeds of $n/n_d = 1.00$ and 1.18, the values of $\bar{\omega}_{min}$ fell within the band, but at the higher speeds the coordinates were considerably displaced. In contrast, the curve of $\bar{\omega}_{\eta max}$ remained relatively close to the limiting band throughout the entire speed range. This indicates that, although the minimum value of relative loss coefficient is used as a reliable parameter in evaluating rotor performance, it can sometimes be misleading as in the case of the subject rotor.

At the tip section, the $\bar{\omega}_{min}$ and $\bar{\omega}_{\eta max}$ increased rapidly when the values of C_p were about 0.45 and 0.50, respectively. The corresponding inlet relative Mach numbers were 0.96 and 0.93. A low-loss C_p range between 0.37 and 0.43 was established in reference 6 from the tip-section data of several transonic rotors.

At the mean and hub sections where the loading was less severe, higher limiting values of C_p were realized with lower losses involved.

The effects of inlet-relative Mach number on relative total-pressure-loss coefficient have already been discussed and are plotted in figure 17 merely as an aid in evaluating their direction relationship without having to cross-plot from the blade-element characteristics. It should be noted

that at inlet relative Mach numbers greater than about 0.95 the values of minimum relative total-pressure-loss coefficient increased rapidly.

Effect of Exit-Annulus Contraction on Performance

The rotor reported in this paper is the rotor of references 2 and 3 with the exception of a 0.3-inch hub buildup which appears in the subject rotor. The modification was made in an attempt to reduce the high diffusion that was required at the tip section of the referenced rotor. In order to evaluate the effects of the hub buildup, the performance of the two rotors is compared. For identification purposes, the subject rotor is referred to as the contracted rotor, and the referenced rotor is called the uncontracted rotor. The performance curves for the uncontracted rotor shown in figures 18 to 24 were taken from the blade-element performance data of reference 3.

The speeds at which the performances were compared were not exactly the same for both rotors but were so close that any change in performance that might have been caused by the difference in speed was considered negligible. Since the two rotors were tested in the same compressor test stand (fig. 4) under similar operating techniques, a comparison of the performance of the two rotors is valid even though blade-element efficiencies exceeding 100 percent were obtained in some cases for the contracted rotor.

Comparison of blade loading.- Figures 18 and 19 present for both rotors the tip-section plots of $\bar{\omega}_{min}$ and $\bar{\omega}_{\eta max}$ as a function of D. At all speeds for the uncontracted rotor, there was close agreement between the diffusion factors corresponding to $\bar{\omega}_{min}$ and the diffusion factors corresponding to $\bar{\omega}_{\eta max}$, but for the contracted rotor there was a decided difference at the higher speeds.

In figures 18 and 19, the diffusion factors for the contracted rotor were lower for all speeds and the corresponding relative total-pressure-loss coefficients were lower at speeds greater than $n/n_d = 1.18$. However, the values in figure 18 are dispersed to a much greater degree than they are in figure 19, especially at the higher speeds.

Figure 20 presents a comparison of the variation in relative total-pressure-loss coefficient with angle of attack. The comparison was made at all three radial locations at design speed (design angles of attack are noted on the plots by vertical arrows on the abscissa).

At speeds greater than design, it was seen that the minimum relative loss coefficient was not in phase with the peak efficiency at the tip

section. However, at design speed, η_{max} and $\bar{\omega}_{min}$ were in phase at all three radial locations (figs. 13, 14, and 15); therefore, figure 20 is considered to be a reliable comparison plot. The relative total-pressure-loss coefficients for the contracted rotor were equal to or lower than the corresponding values for the uncontracted rotor with the exception of the minimum angle-of-attack position at the tip section.

Comparison of axial-velocity ratio.- The original uncontracted rotor experienced a radial flow shift associated with tip separation, in much the same manner as the contracted rotor. In order for the effects of the hub contraction on the flow shift to be examined more closely, data were plotted to show a comparison between the axial-velocity ratios for the two rotors at the tip, mean, and hub sections (figs. 21, 22, and 23). The comparison is made in the direction of the flow shift or from the tip section to the hub section.

Both rotors experienced a drop in axial velocity across the rotor tip which became more pronounced with speed increase. The uncontracted rotor had an axial-velocity ratio of 0.83 at design speed and maximum weight flow, and with increasing speed it dropped continuously to a minimum of 0.32 near stall at a speed of $n/n_d = 1.43$. The contracted rotor had an axial-velocity ratio of 1.02 at design speed and maximum weight flow and a ratio of 0.47 near stall at a speed of $n/n_d = 1.45$. The change in the axial-velocity ratios was 0.51 and 0.55 for the uncontracted and the contracted rotors, respectively. At the tip, therefore, the contraction had little effect on the rate of axial-velocity decrease, but it had a definite effect on the level. That is, the tip of the contracted rotor passed more flow, and this was to be expected in view of its smaller exit annulus.

At the mean section, both rotors exhibited about the same trends in axial-velocity ratio with the level of the curves again being somewhat higher for the contracted rotor. The curves rose and fell slightly, but generally the axial-velocity ratio remained fairly constant at the mean section of each rotor.

At the hub section, the axial-velocity ratio for the uncontracted rotor increased with angle of attack for speeds of $n/n_d = 0.99$ and 1.16, but at the higher speeds no appreciable velocity rise was detected. For the contracted rotor, the velocity ratio displayed a rise throughout the whole speed range.

When separation occurred at the tip of the subject rotor and the flow started to shift towards the hub, it was restricted by the 0.3-inch hub buildup. As a result, the tip section was forced to pass more flow than it ordinarily would had the hub not been contracted. This is confirmed

by the fact that at the two highest speeds the axial-velocity ratio at the tip of the contracted rotor began to rise at high angles of attack whereas it continued to fall in the uncontracted rotor.

Comparison of overall performance.- For all speeds throughout most of the operating range of the compressor, the contracted rotor had a higher overall efficiency than the uncontracted rotor (fig. 24). Choking occurred at lower weight flows for the contracted rotor because of the smaller exit annular area. But in spite of this, the hub buildup had the effect of increasing the operating range of the compressor because it allowed the rotor to go to higher angles of attack before the onset of stall.

The total-pressure ratio of the contracted rotor was equal to or greater than the pressure ratio of the uncontracted rotor in the regions of low weight flow (near surge). In the vicinity of high weight flow and especially at high speed, the overall total-pressure ratio was lower for the contracted rotor because the operation in that region was choked. The maximum total-pressure ratio was 1.54 for the uncontracted rotor in comparison with 1.60 for the contracted rotor. The highest efficiency, as indicated in these comparison curves, for the uncontracted rotor was 92 percent, whereas that for the contracted rotor was 96 percent.

SUMMARY OF RESULTS

An investigation was conducted on a transonic compressor rotor having a reduced exit annulus and blades cambered in accordance with the NACA A_2I_{8b} mean-line series. This rotor embodies a modification of a previously investigated rotor (NACA Research Memorandum L57H08). The following results were obtained:

1. The overall design total-pressure ratio was attained at a mean section angle of attack 4.5° greater than the low-speed design value taken from two-dimensional cascade data.

2. Peak blade-element efficiency for all speeds and all radial locations occurred in an angle-of-attack range from 3° to 8.5° above design.

3. At design and 118 percent of design speed, the flow turning produced at the mean and tip sections was in close agreement with low-speed cascade turning data at low angles of attack.

4. Minimum relative total-pressure-loss coefficient for the hub, mean, and tip sections increased rapidly when the inlet relative Mach number became greater than about 0.95. The highest inlet relative Mach number was 1.27.

5. Relative total-pressure-loss coefficient at design speed started to rise at the tip section at a diffusion factor of about 0.48.

6. At speeds greater than 118 percent of design, the tip-section values of minimum total-pressure-loss coefficient did not occur when the efficiency was a maximum. It is believed that the rapid rise in pressure ratio more than compensated for the effects of the rise in relative total-pressure-loss coefficient.

7. The operating range of the compressor was increased by the reduction in exit annulus.

8. For speeds throughout most of the operating range, the reduction in exit annulus had the effect of increasing the overall rotor efficiency.

9. The high diffusion that was required at the rotor tip was reduced by contracting the exit annulus.

Langley Aeronautical Laboratory,
National Advisory Committee for Aeronautics,
Langley Field, Va., November 8, 1957.

REFERENCES

1. Erwin, John R., Savage, Melvyn, and Emery, James C.: Two-Dimensional Low-Speed Cascade Investigation of NACA Compressor Blade Sections Having a Systematic Variation in Mean-Line Loading. NACA TN 3817, 1956. (Supersedes NACA RM L53I30b.)

2. Savage, Melvyn, Erwin, John R., and Whitley, Robert P.: Investigation of an Axial-Flow Compressor Rotor Having NACA High-Speed Blade Sections (A_2I_{8b} Series) at Mean Radius Relative Inlet Mach Numbers up to 1.13. NACA RM L53G02, 1953.

3. Bernot, Peter T., and Savage, Melvyn: Transonic Investigation of an Axial-Flow Compressor Rotor With a Hub-Tip Ratio of 0.75 and Blades Having NACA A_2I_{8b} Mean Lines. NACA RM L57H08, 1957.

4. Schulze, Wallace M., Ashby, George C., Jr., and Erwin, John R.: Several Combination Probes for Surveying Static and Total Pressure and Flow Direction. NACA TN 2830, 1952.

5. Godwin, William R.: Distribution of Losses Behind a Compressor Rotor As Measured by a Rotating Rake. NACA RM L55F29, 1955.

6. Felix, A. Richard, and Savage, Melvyn: Investigation of a High-Performance Axial-Flow Compressor Transonic Inlet Rotor Designed for 37.5 Pounds Per Second Per Square Foot of Frontal Area - Detailed Blade-Element Performance. NACA RM L56K23, 1956.

7. Lieblein, Seymour, Schwenk, Francis C., and Broderick, Robert L.: Diffusion Factor for Estimating Losses and Limiting Blade Loadings in Axial-Flow-Compressor Blade Elements. NACA RM E53D01, 1953.

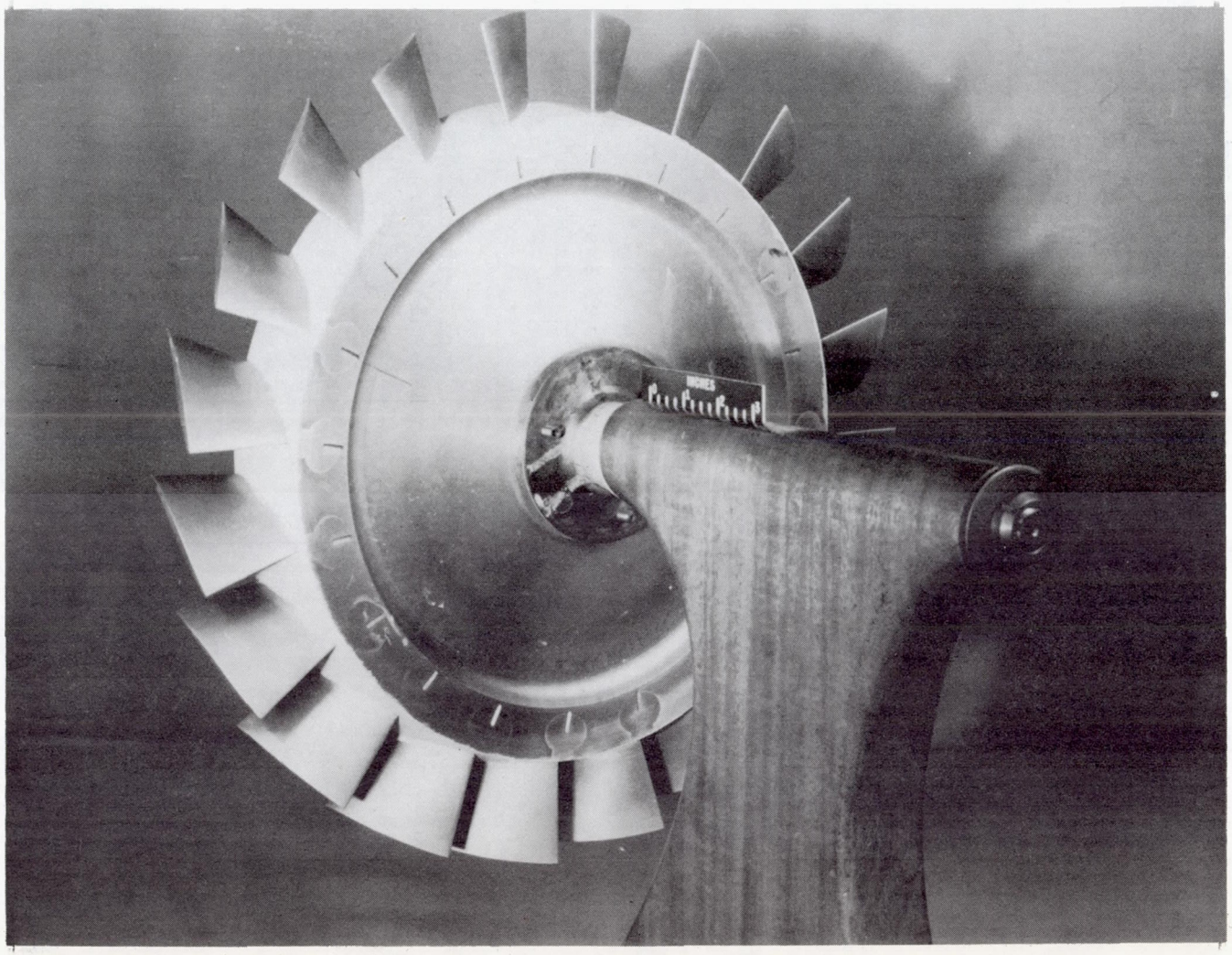

Figure 1.- Compressor rotor with contracted exit annulus. L-57-332

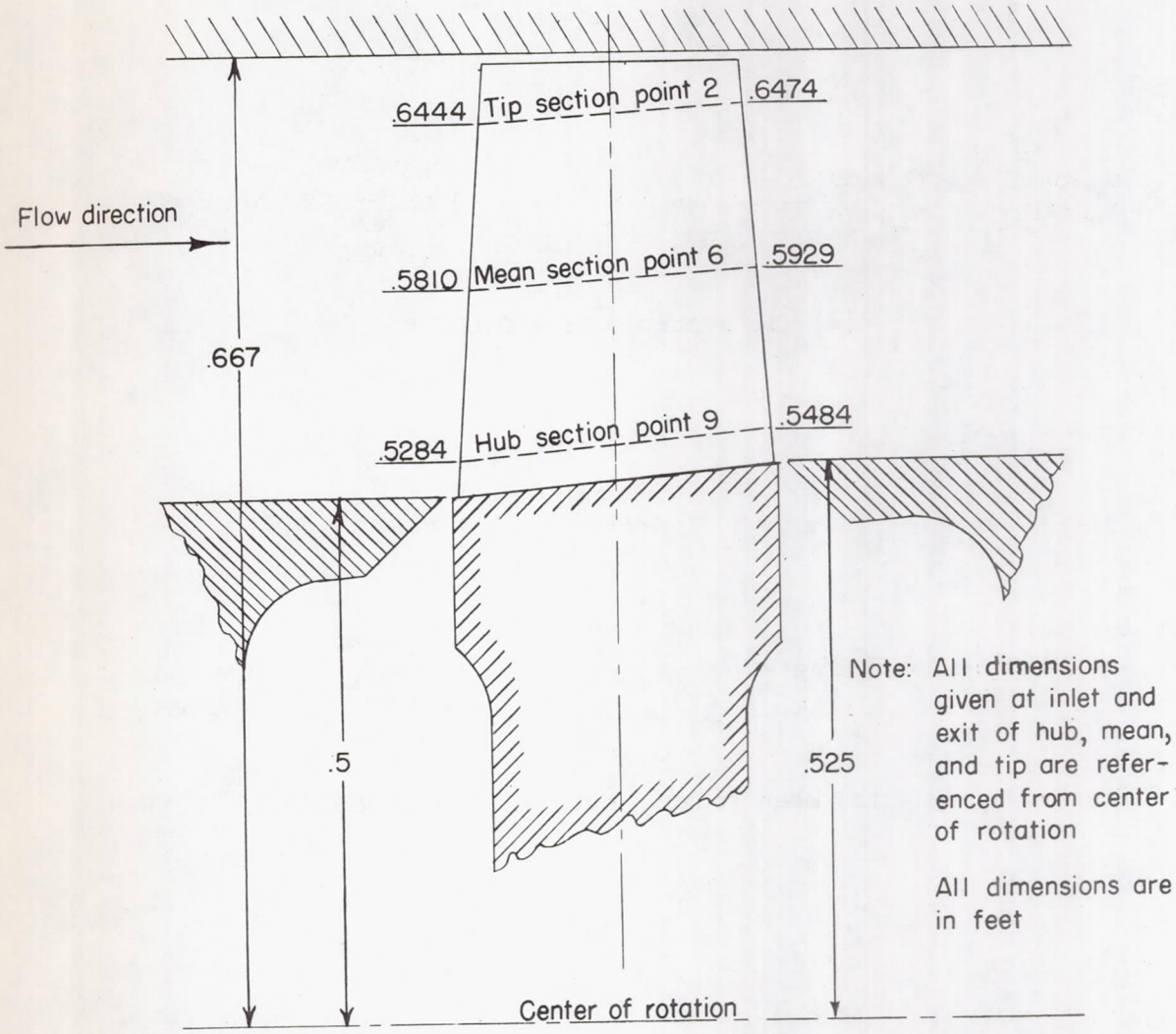

Figure 2.- Schematic drawing of hub contour showing the assumed streamline paths at the hub, mean, and tip sections.

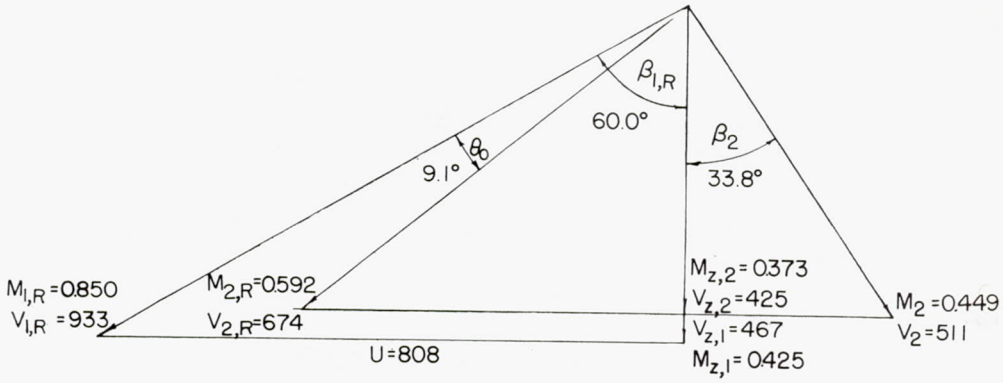

(a) Tip section. r = 0.667 foot.

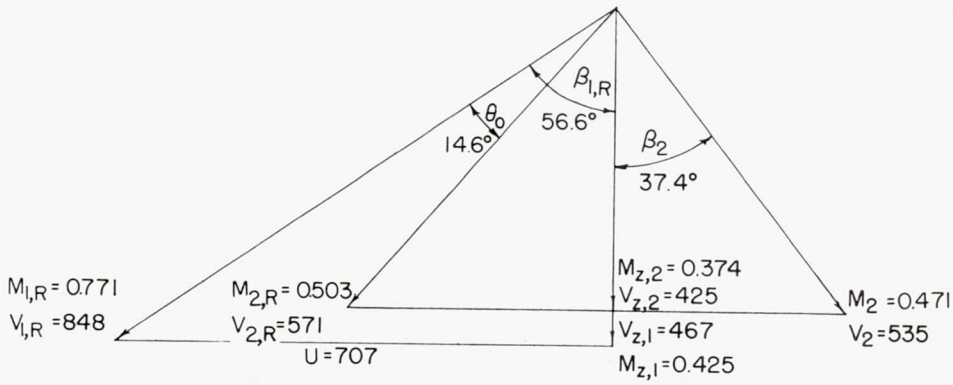

(b) Mean radius section. r = 0.583 foot.

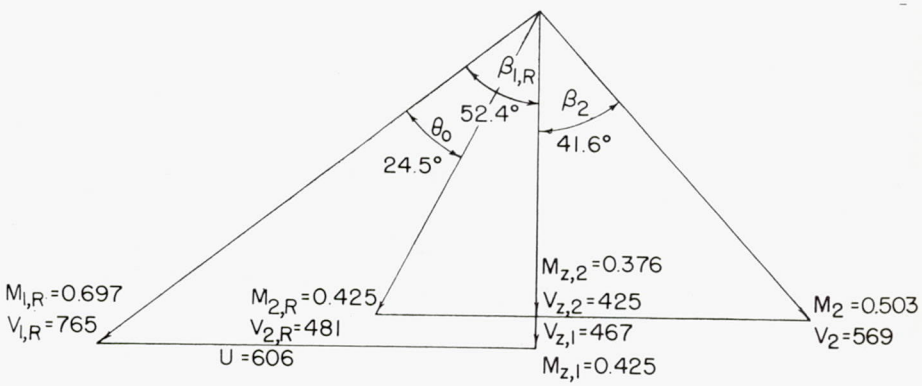

(c) Hub section. r = 0.500 foot.

Figure 3.- Design velocity diagrams in air without the contraction in exit annulus.

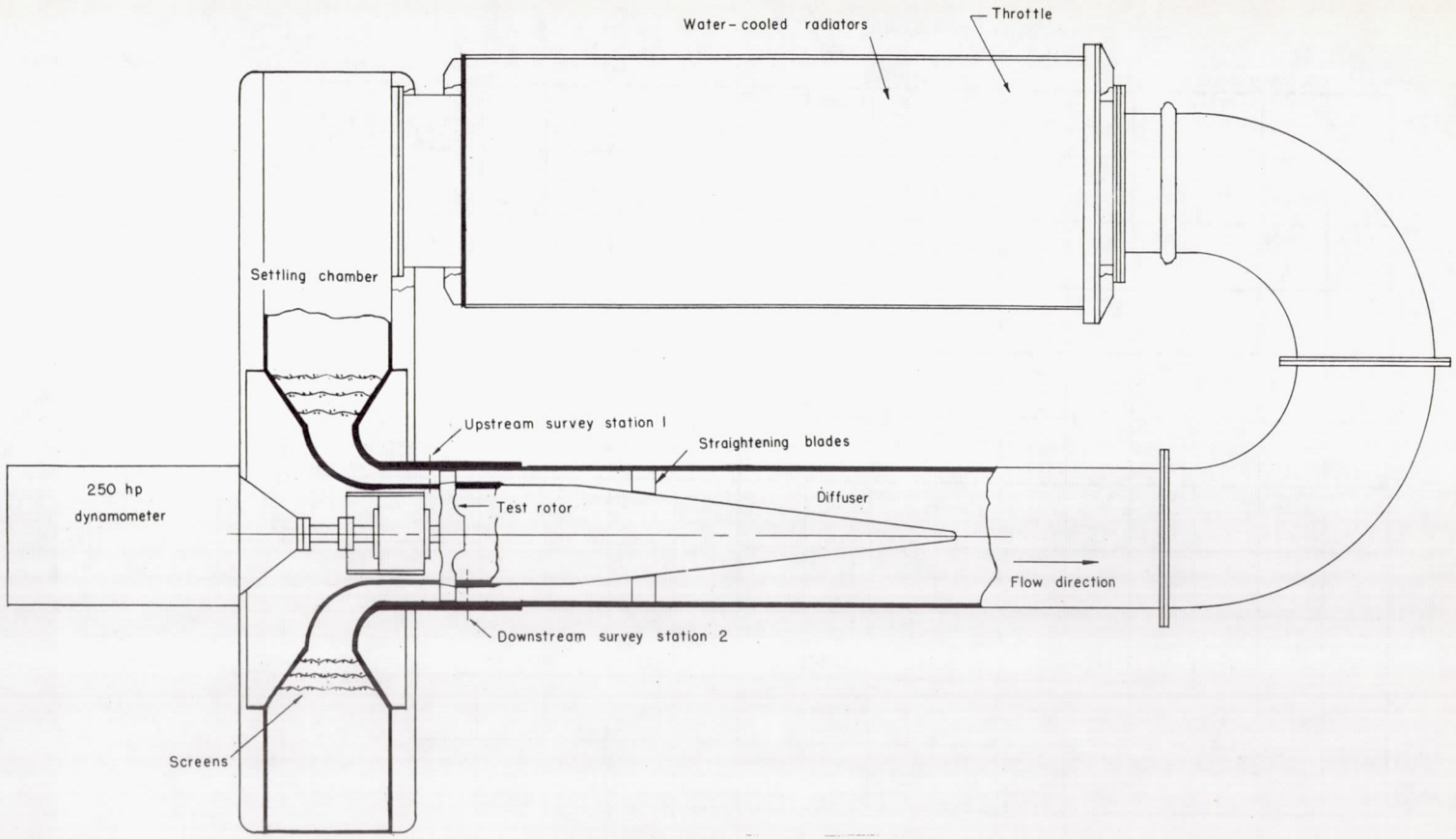

Figure 4.- Schematic drawing of compressor test stand.

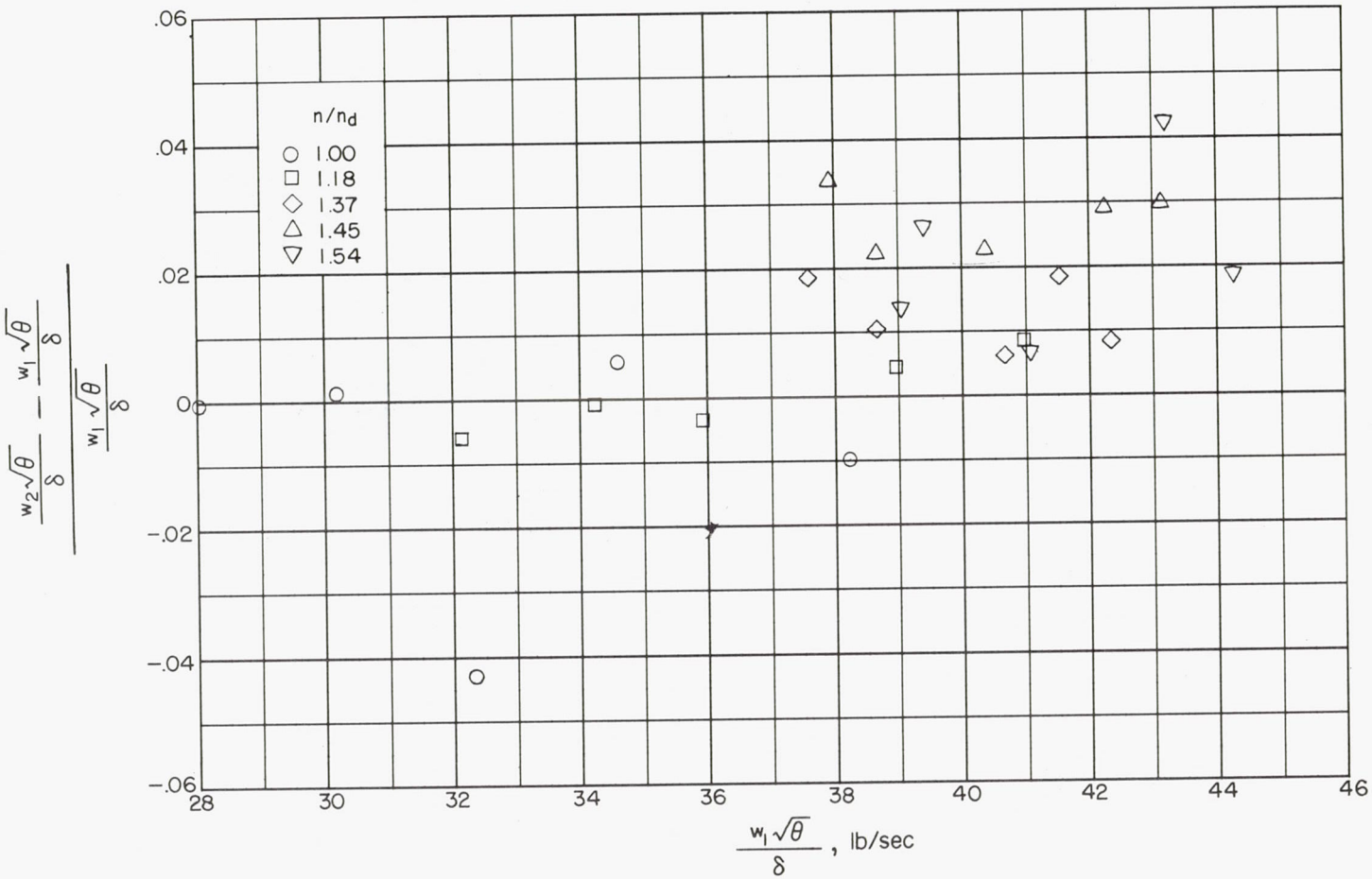

Figure 5.- Comparison of Freon weight-flow measurements at all speeds.

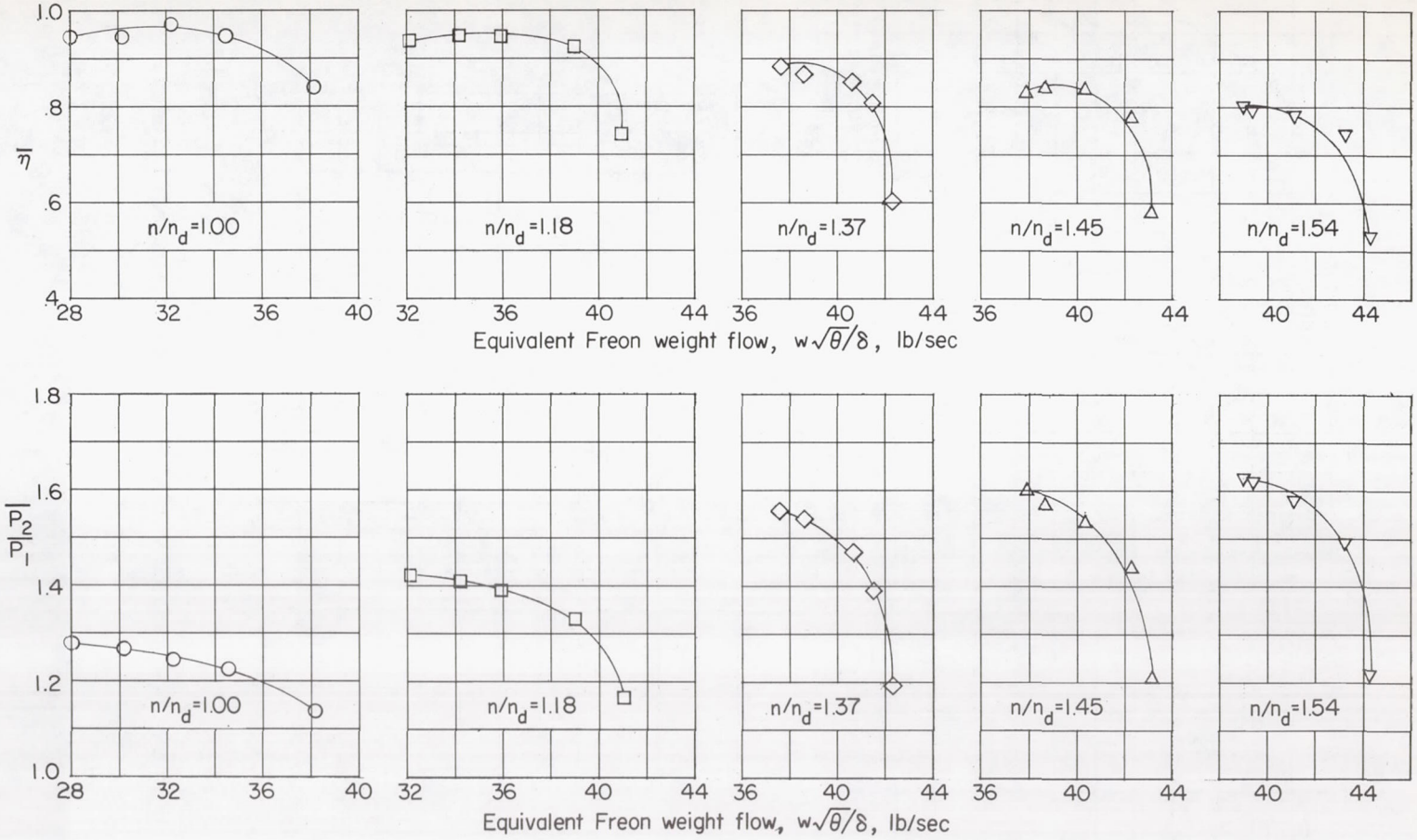

Figure 6.- Overall rotor performance.

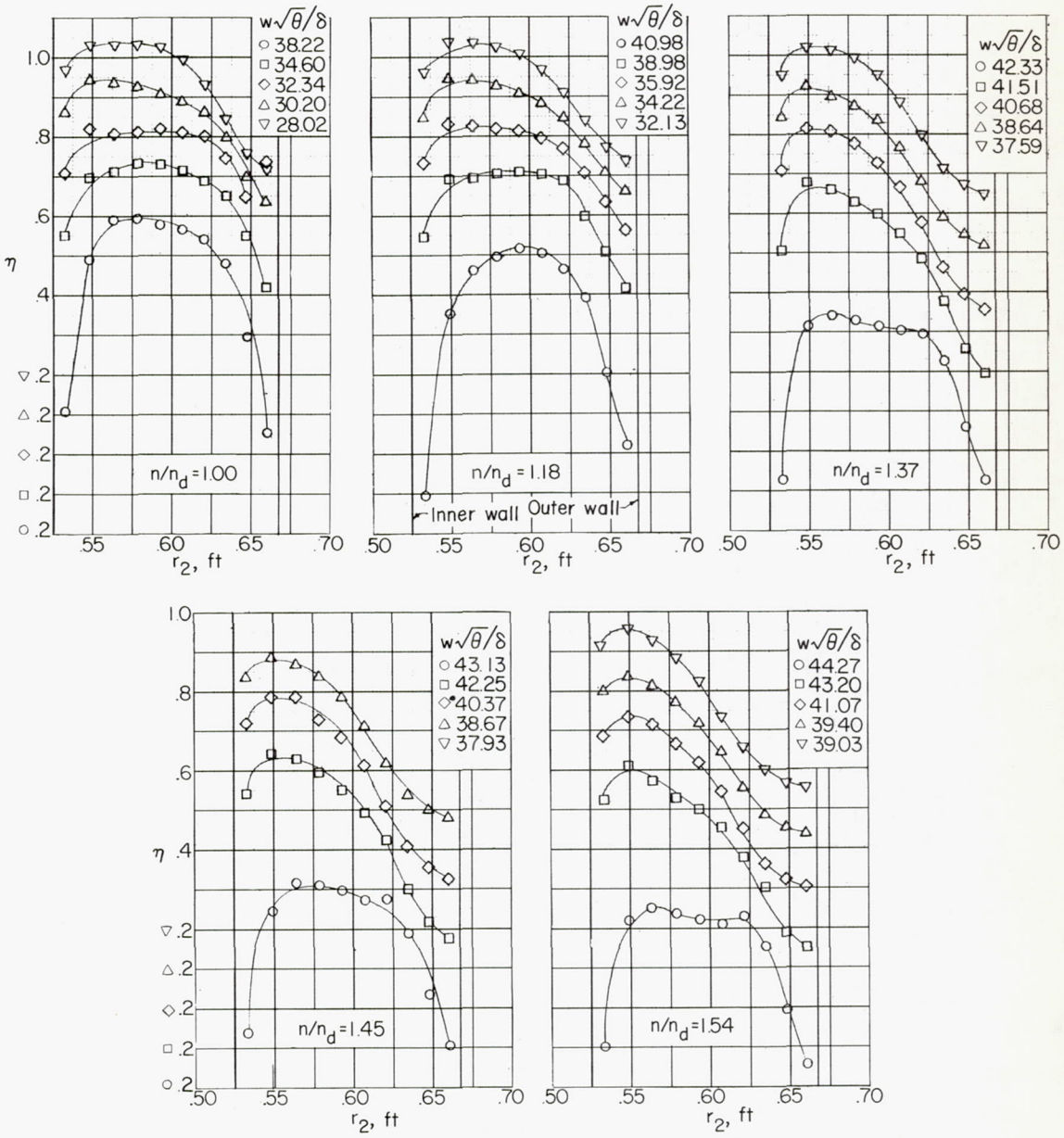

Figure 7.- Radial variation of momentum efficiency.

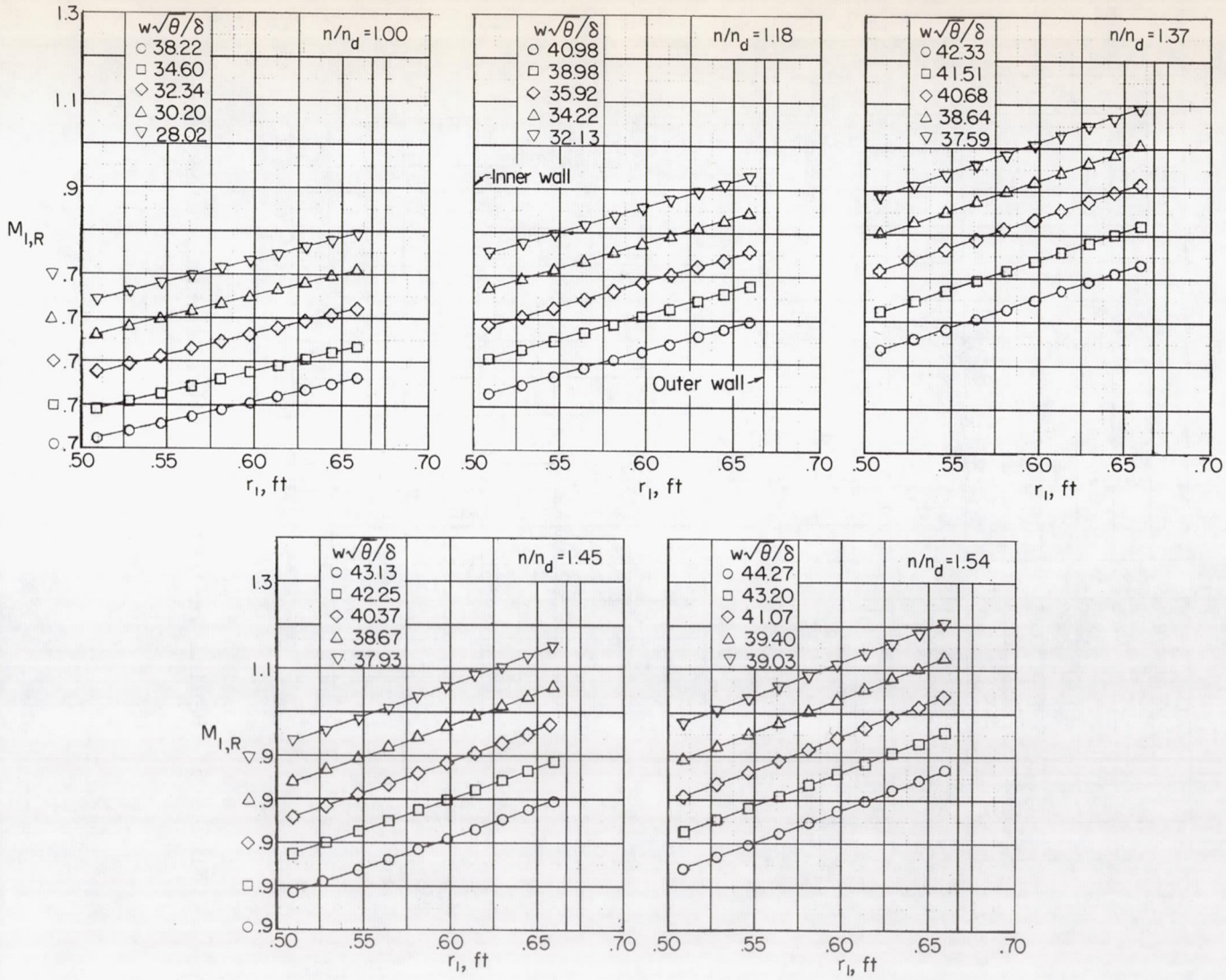

Figure 8.- Radial variation of inlet relative Mach number.

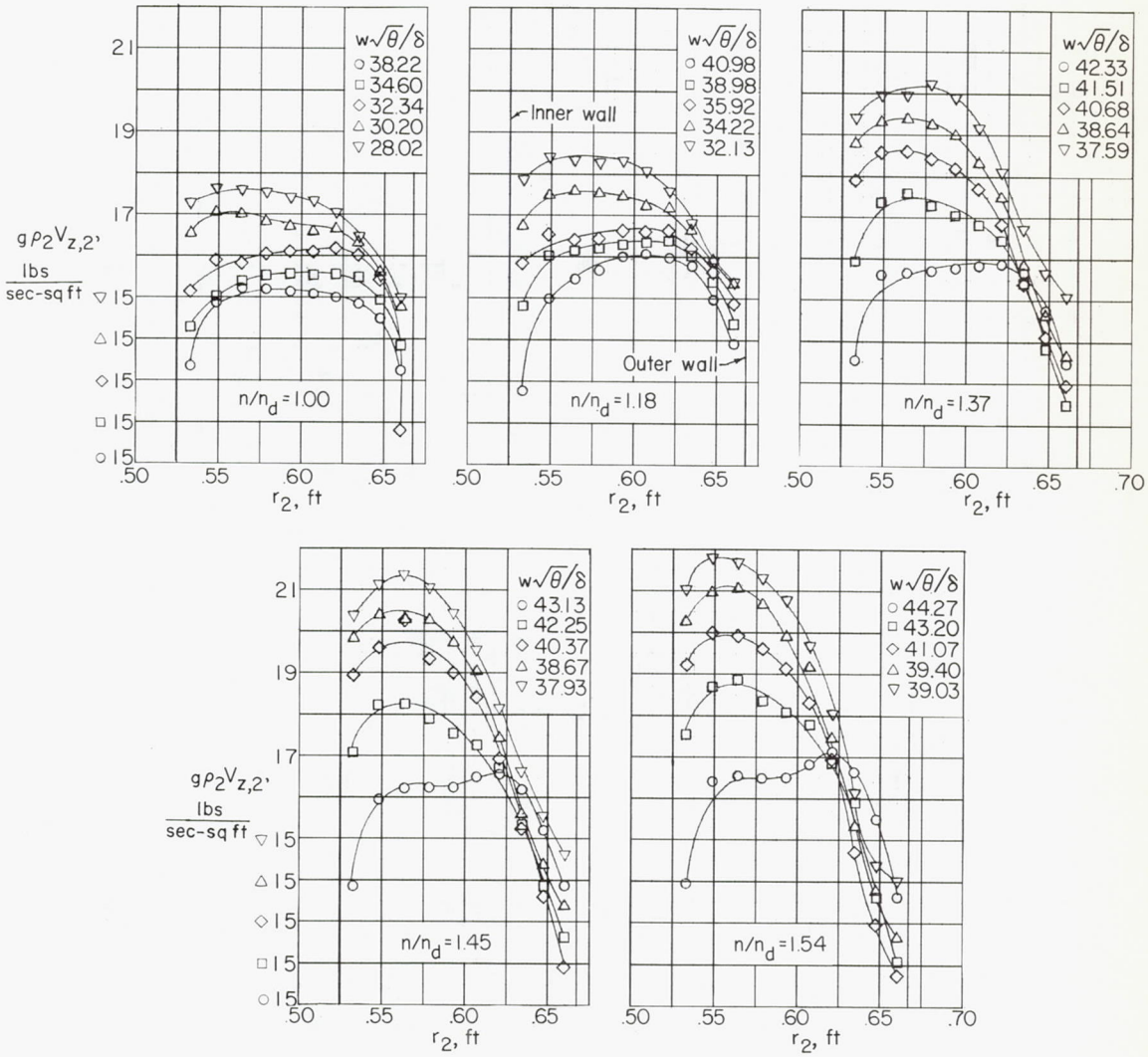

Figure 9.- Radial variation of exit elemental weight flow.

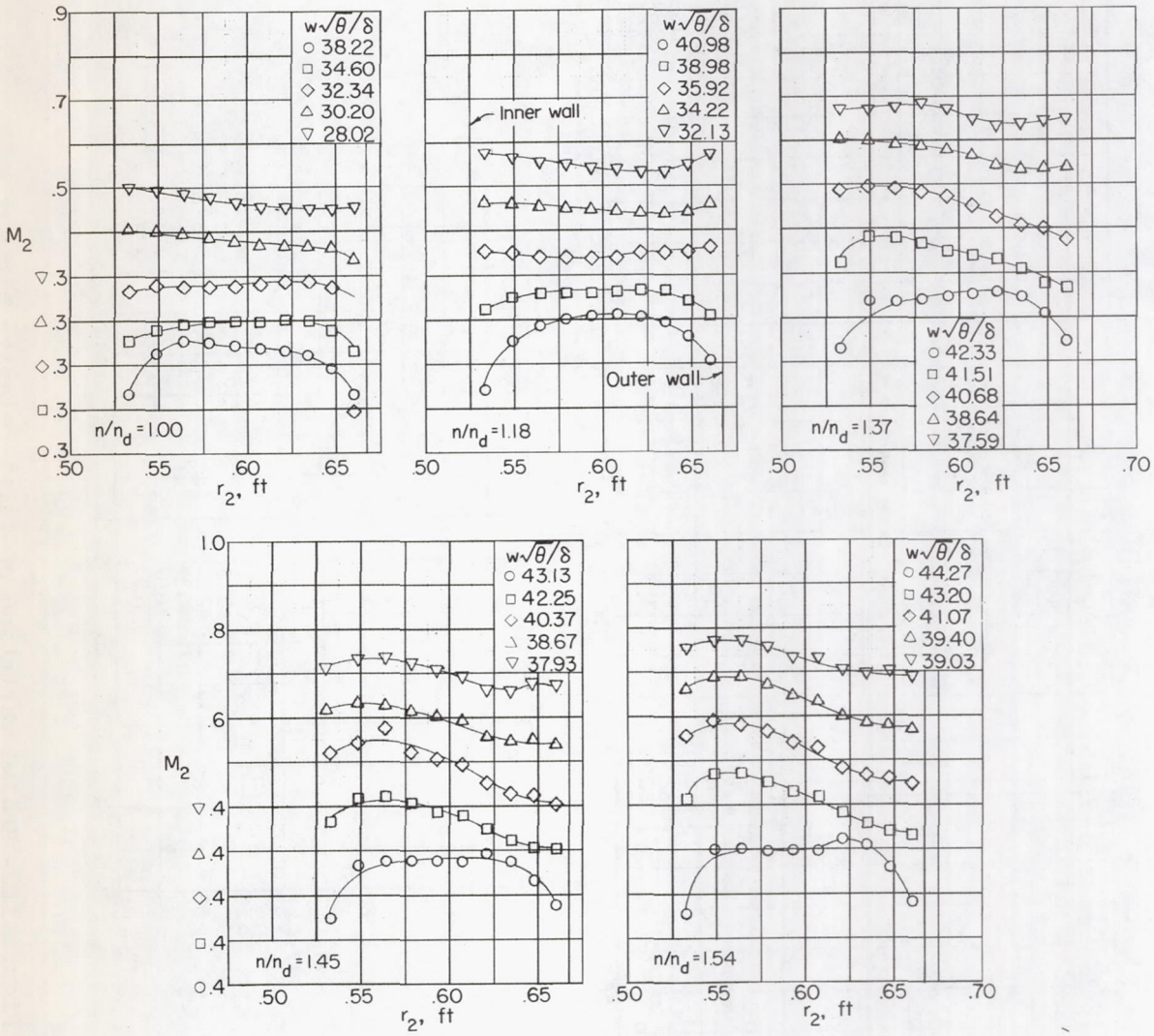

Figure 10.- Radial variation of exit absolute Mach number.

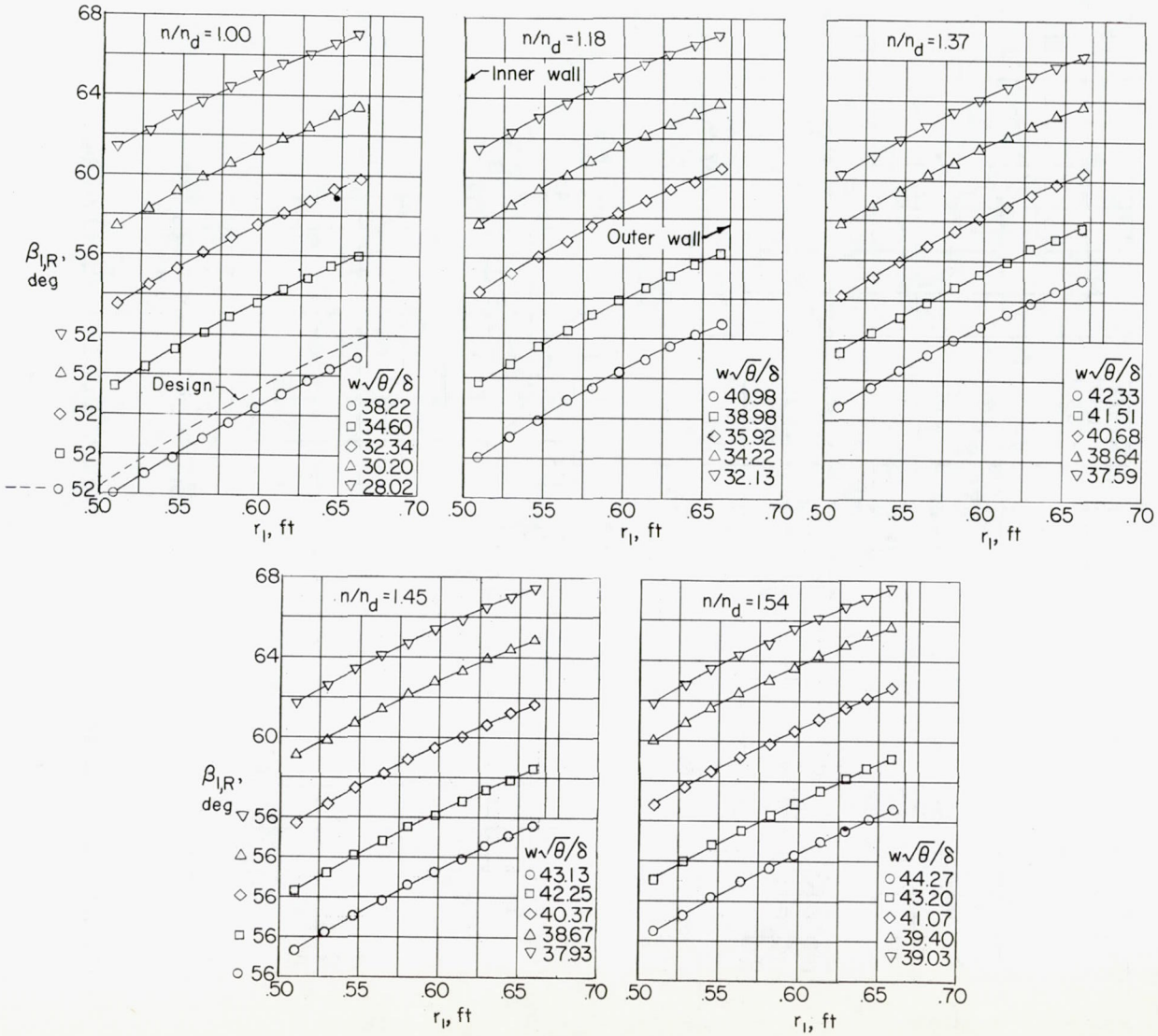

Figure 11.- Radial variation of inlet relative air angle.

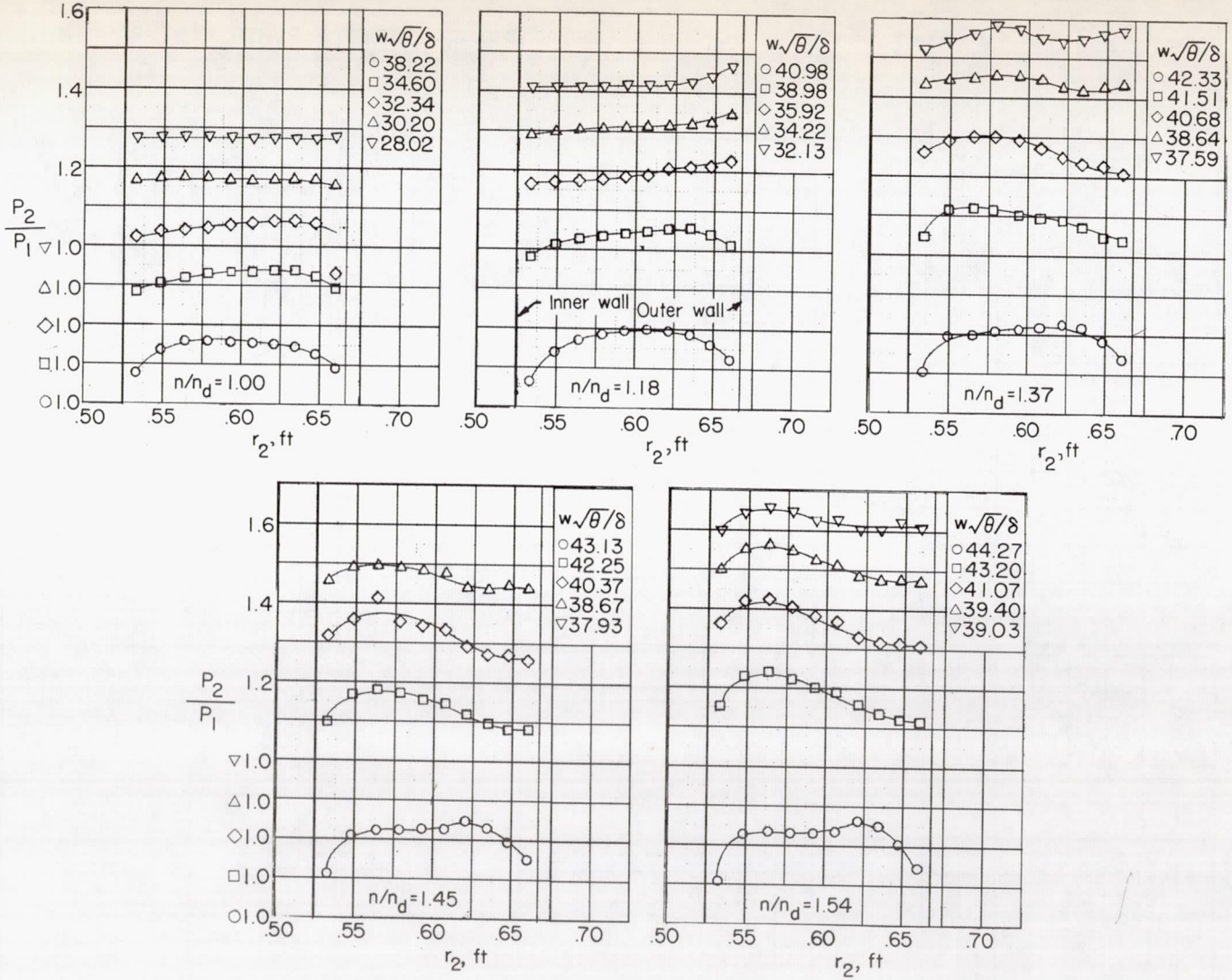

Figure 12.- Radial variation of total-pressure ratio.

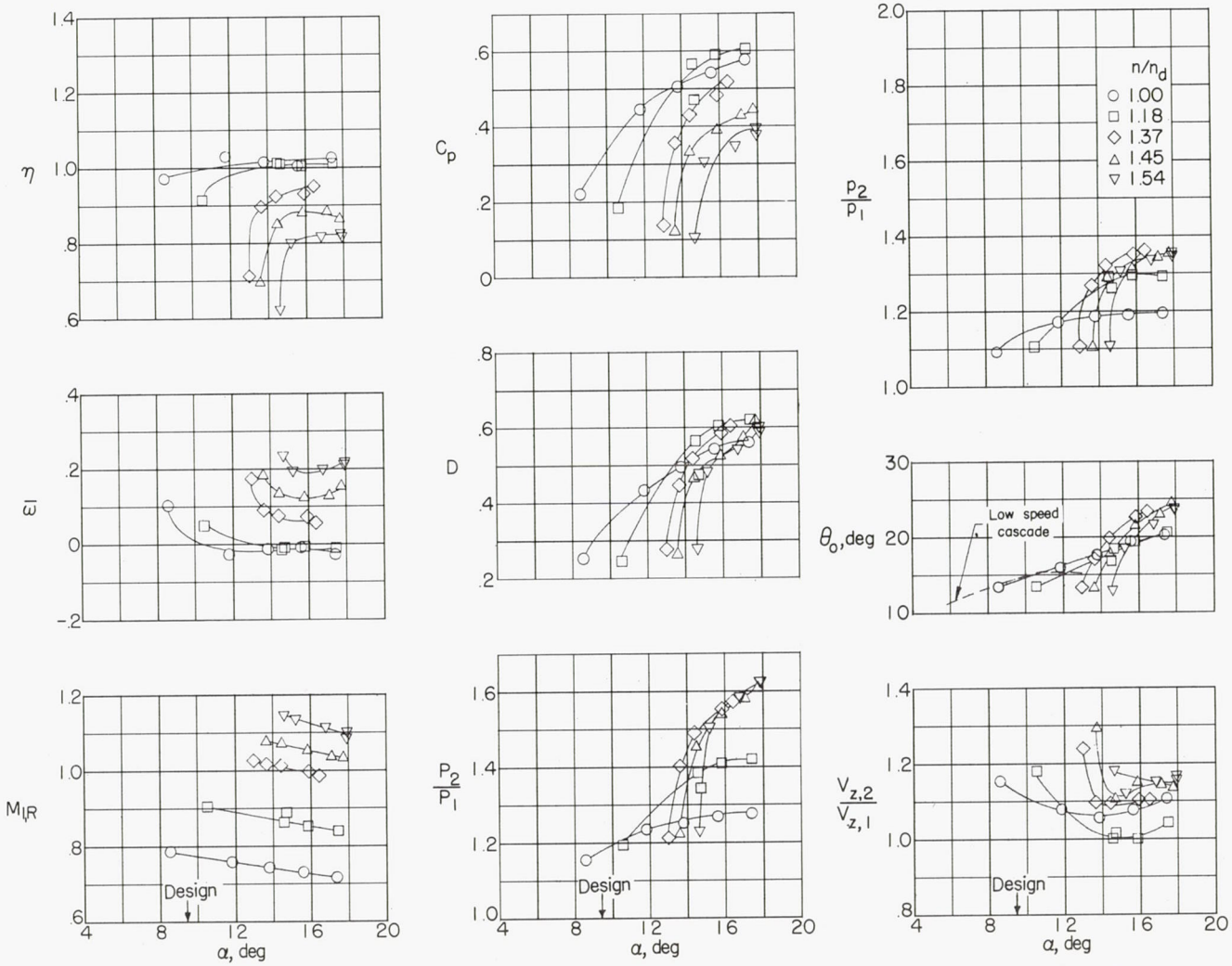

Figure 13.- Blade-element characteristics at the mean section. r_2 = 0.5929 foot.

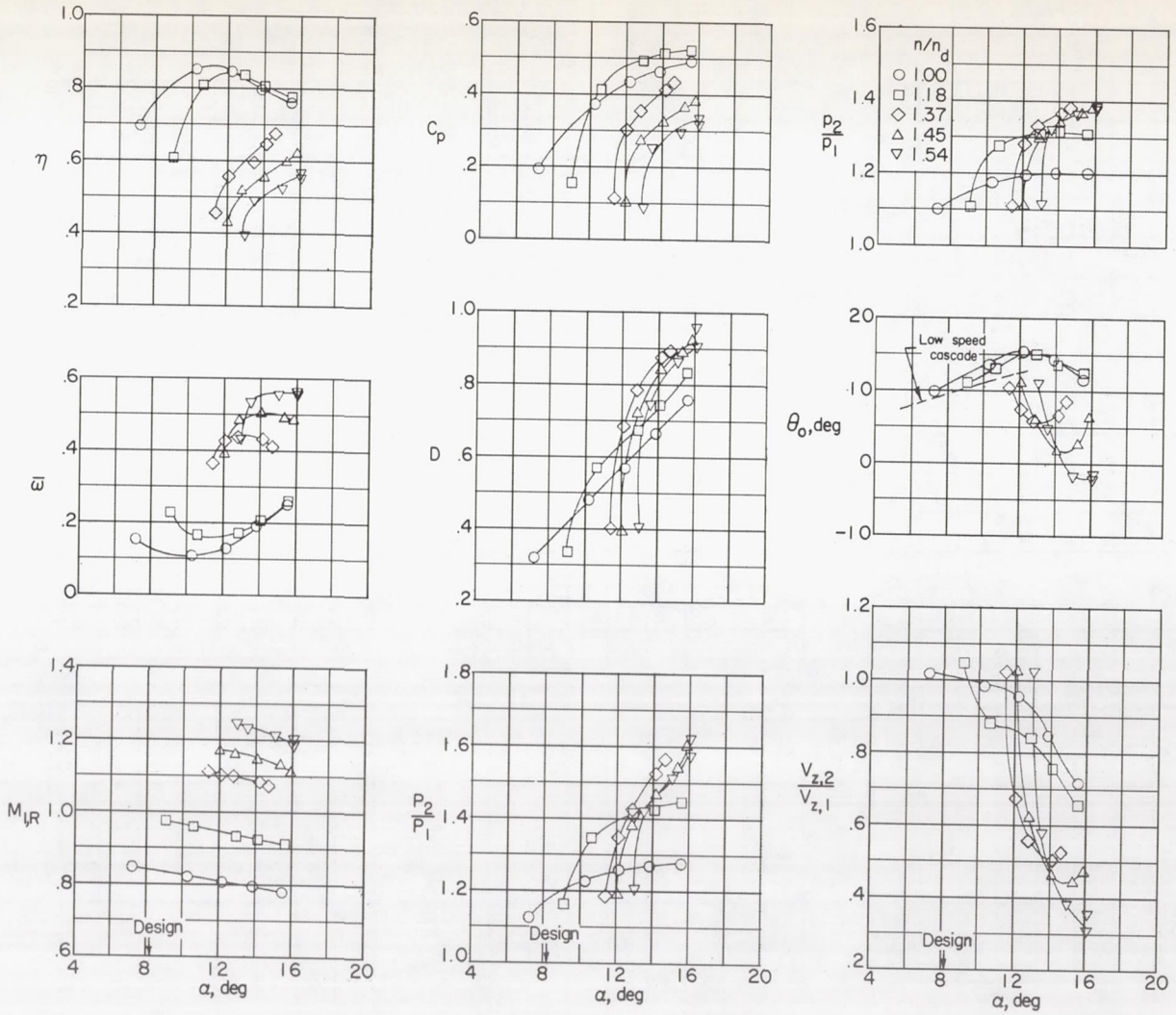

Figure 14.- Blade-element characteristics at the tip section. $r_2 = 0.6474$ foot.

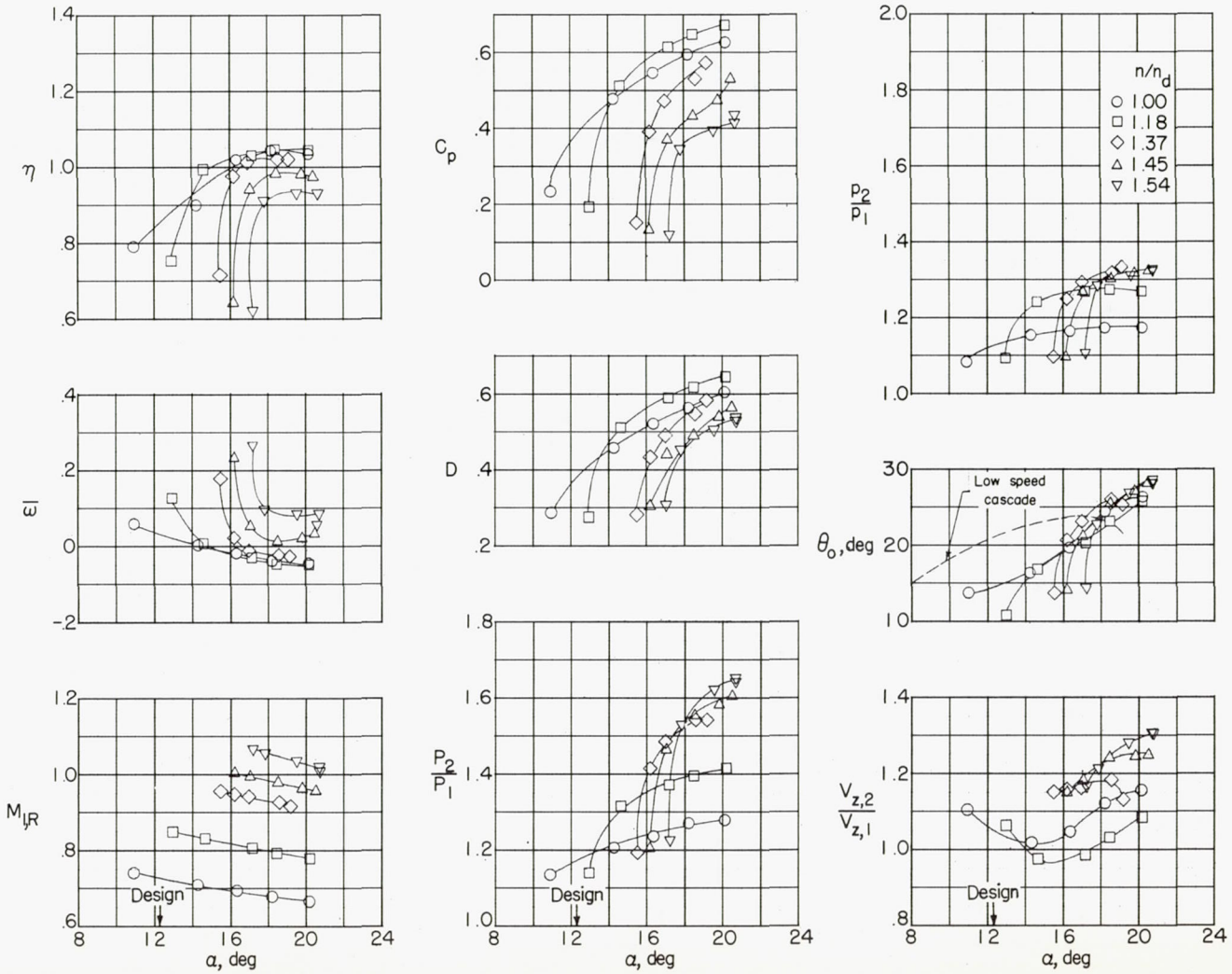

Figure 15.- Blade-element characteristics at the hub section. r_2 = 0.5484 foot.

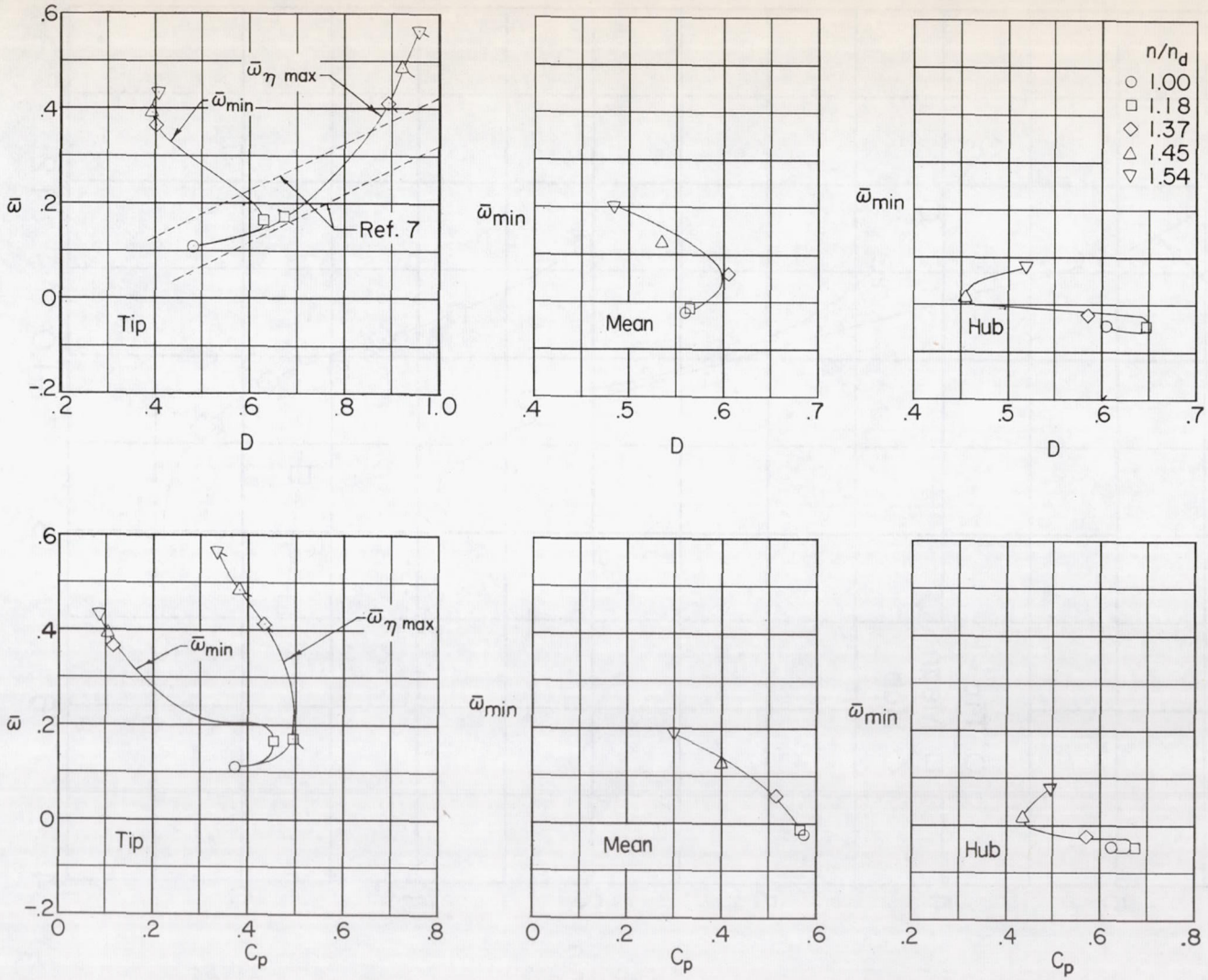

Figure 16.- Variation of relative total-pressure-loss coefficient with respect to diffusion factor and diffusion coefficient.

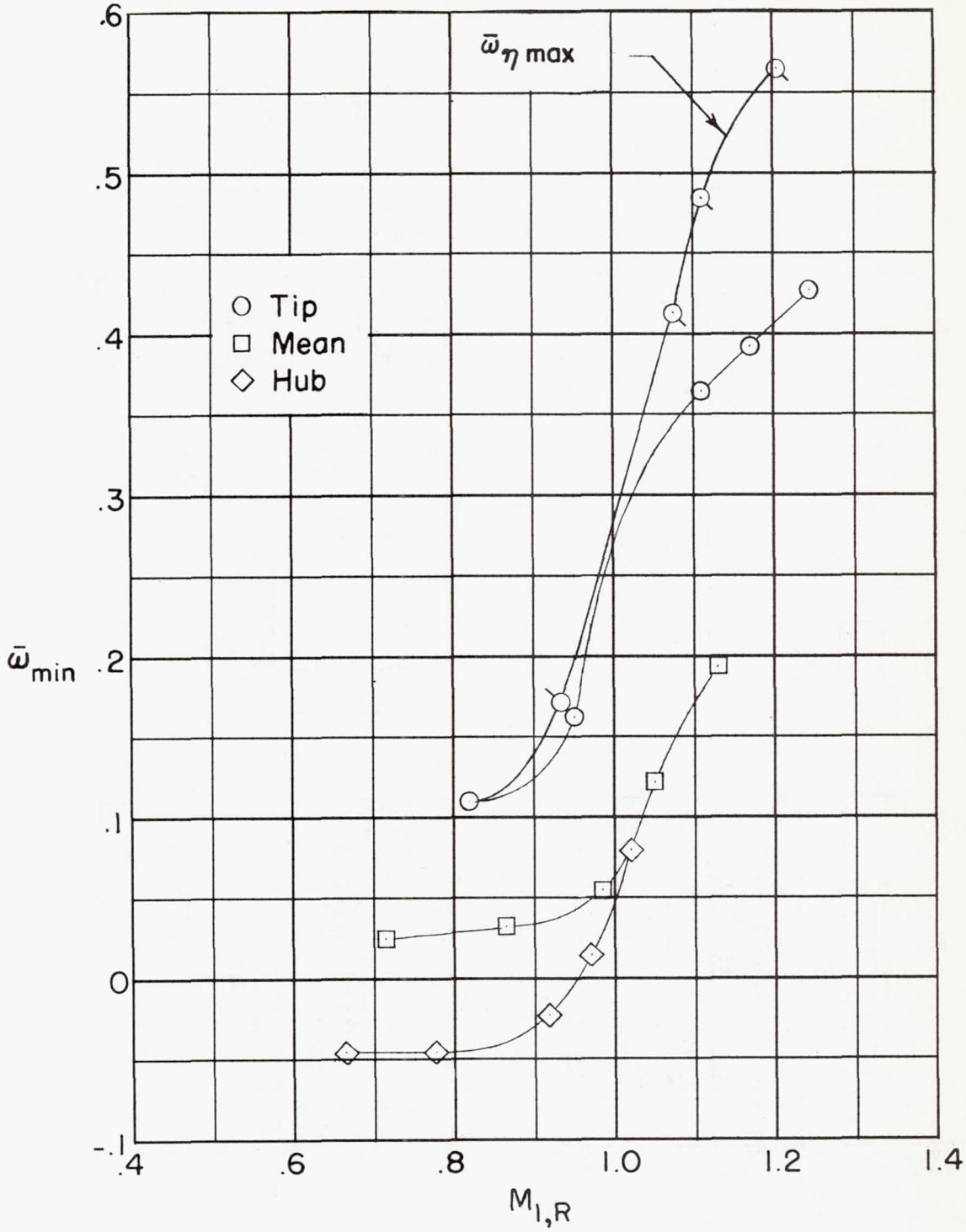

Figure 17.- Variation of relative total-pressure-loss coefficient with respect to inlet relative Mach number.

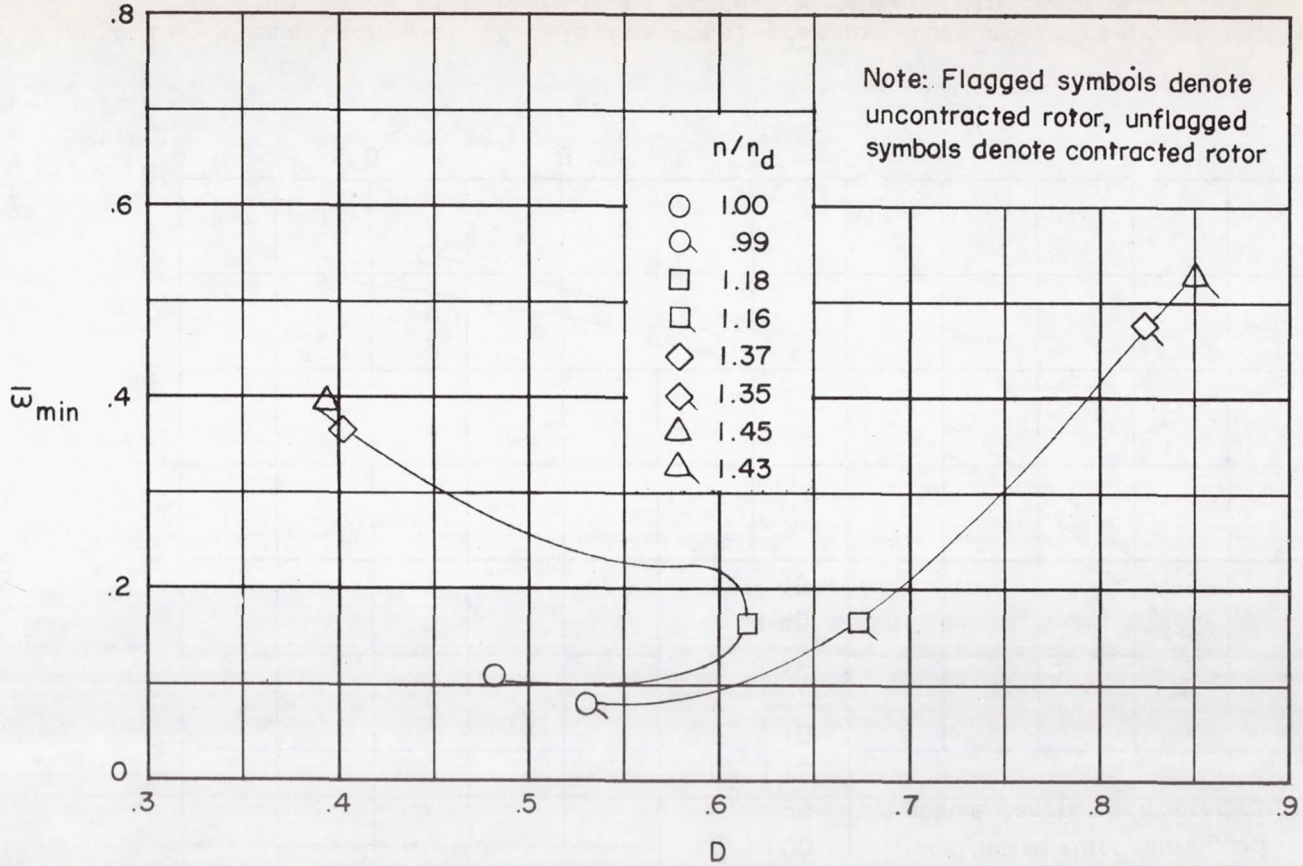

Figure 18.- Comparison plot of the variation of minimum relative total-pressure-loss coefficient with respect to diffusion factor (tip section).

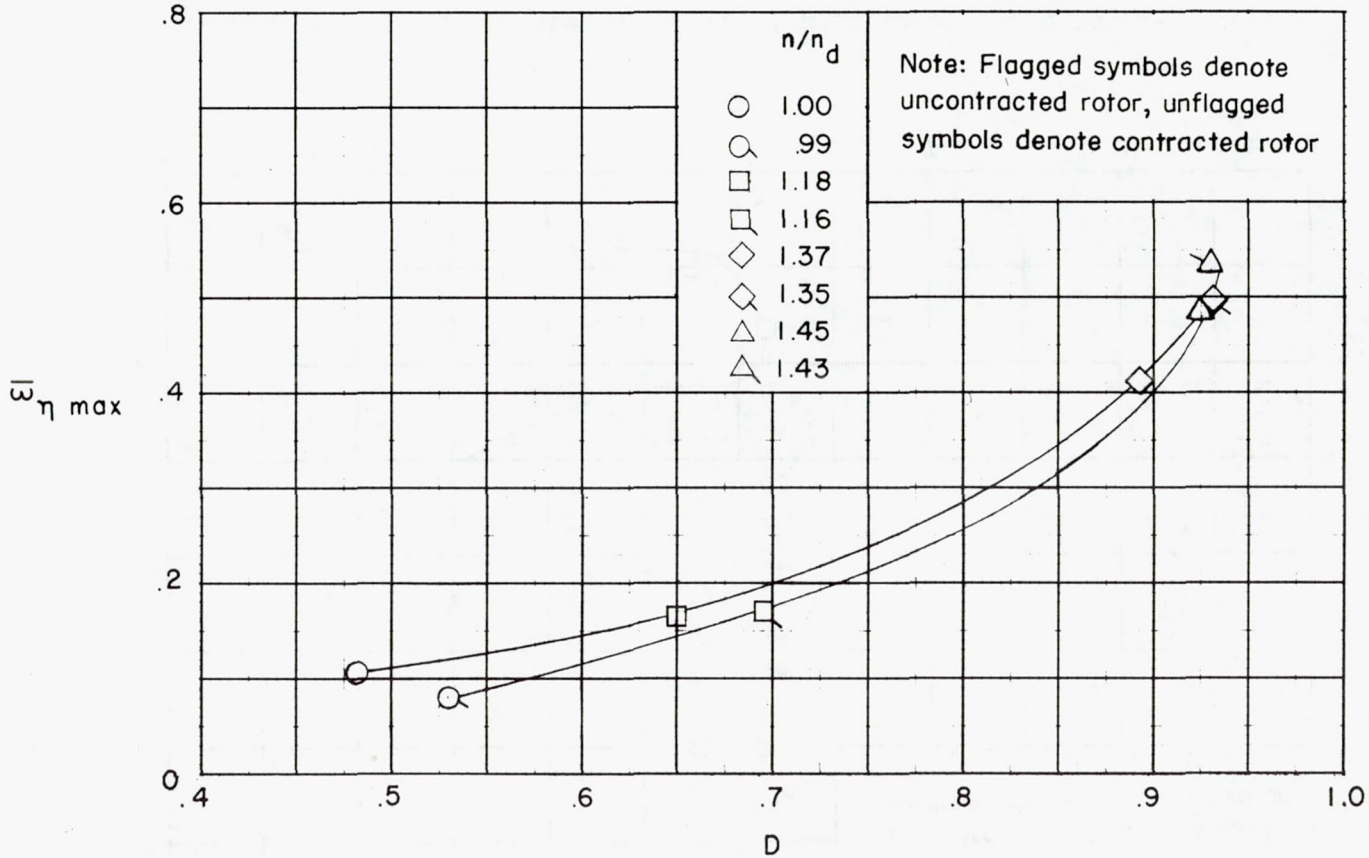

Figure 19.- Comparison plot of relative total-pressure-loss coefficient at maximum efficiency with respect to diffusion factor (tip section).

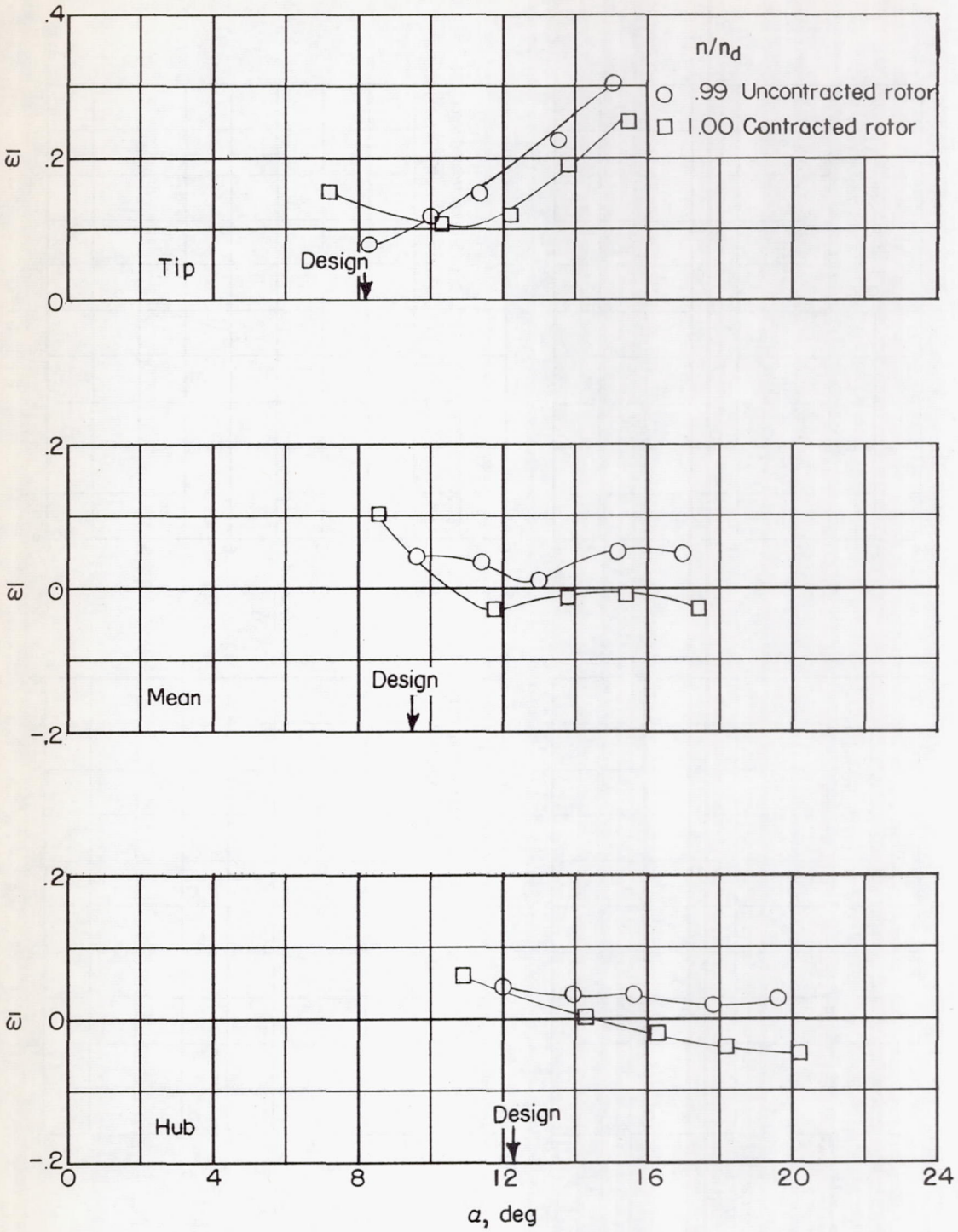

Figure 20.- Comparison plot at design speed of minimum relative total-pressure-loss coefficient with respect to angle of attack.

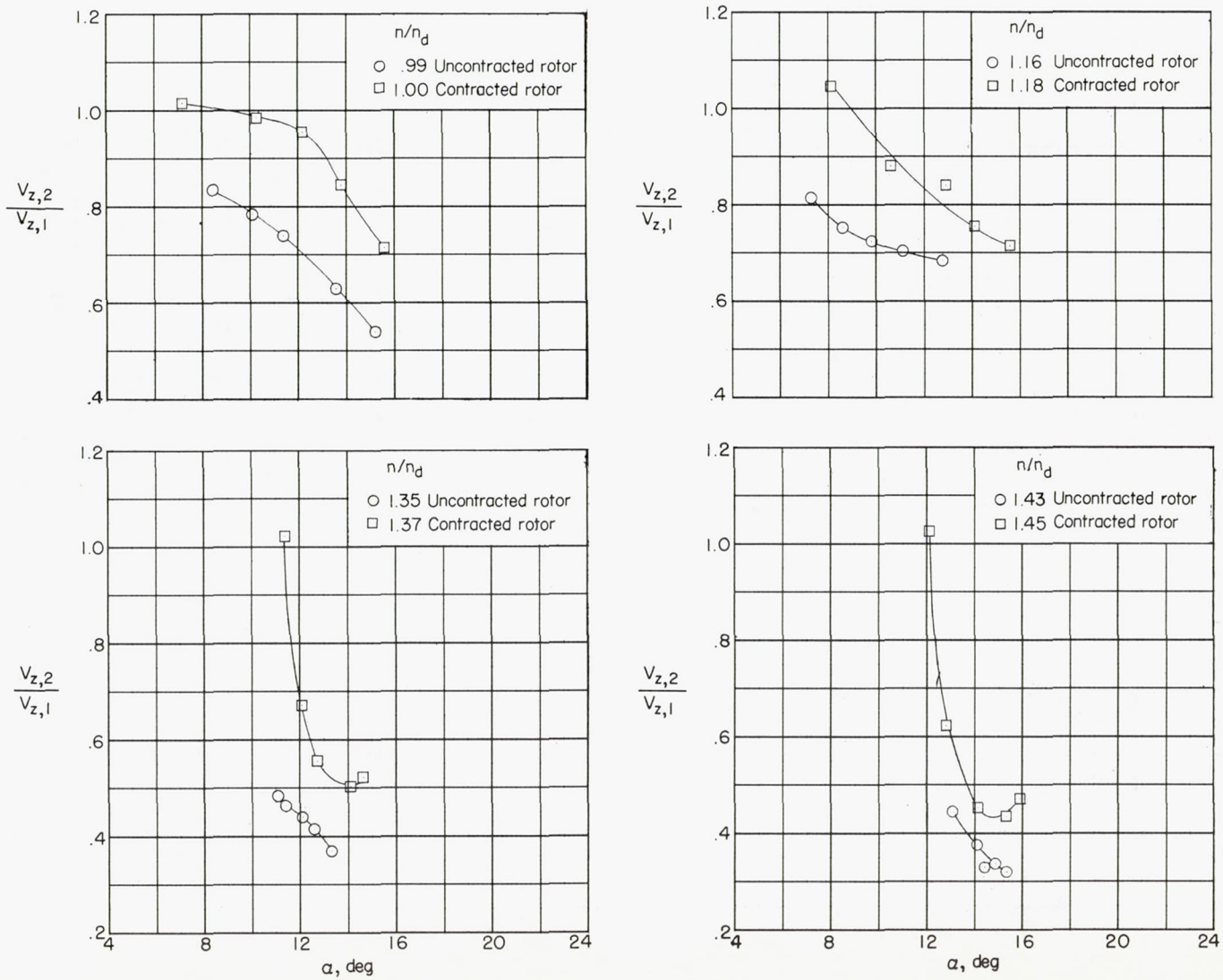

Figure 21.- Comparison of axial-velocity ratio at the tip section.

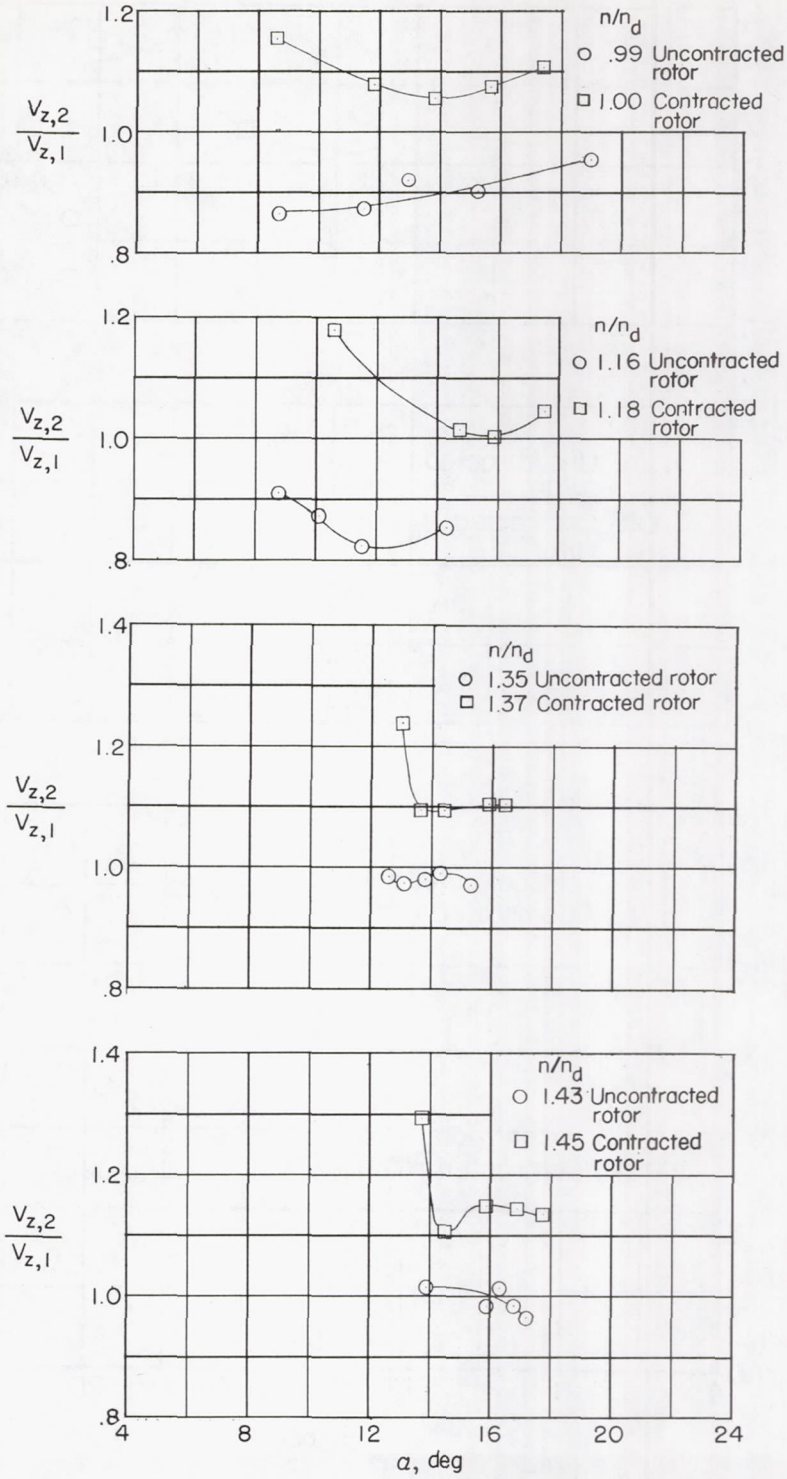

Figure 22.- Comparison of axial-velocity ratio at the mean section.

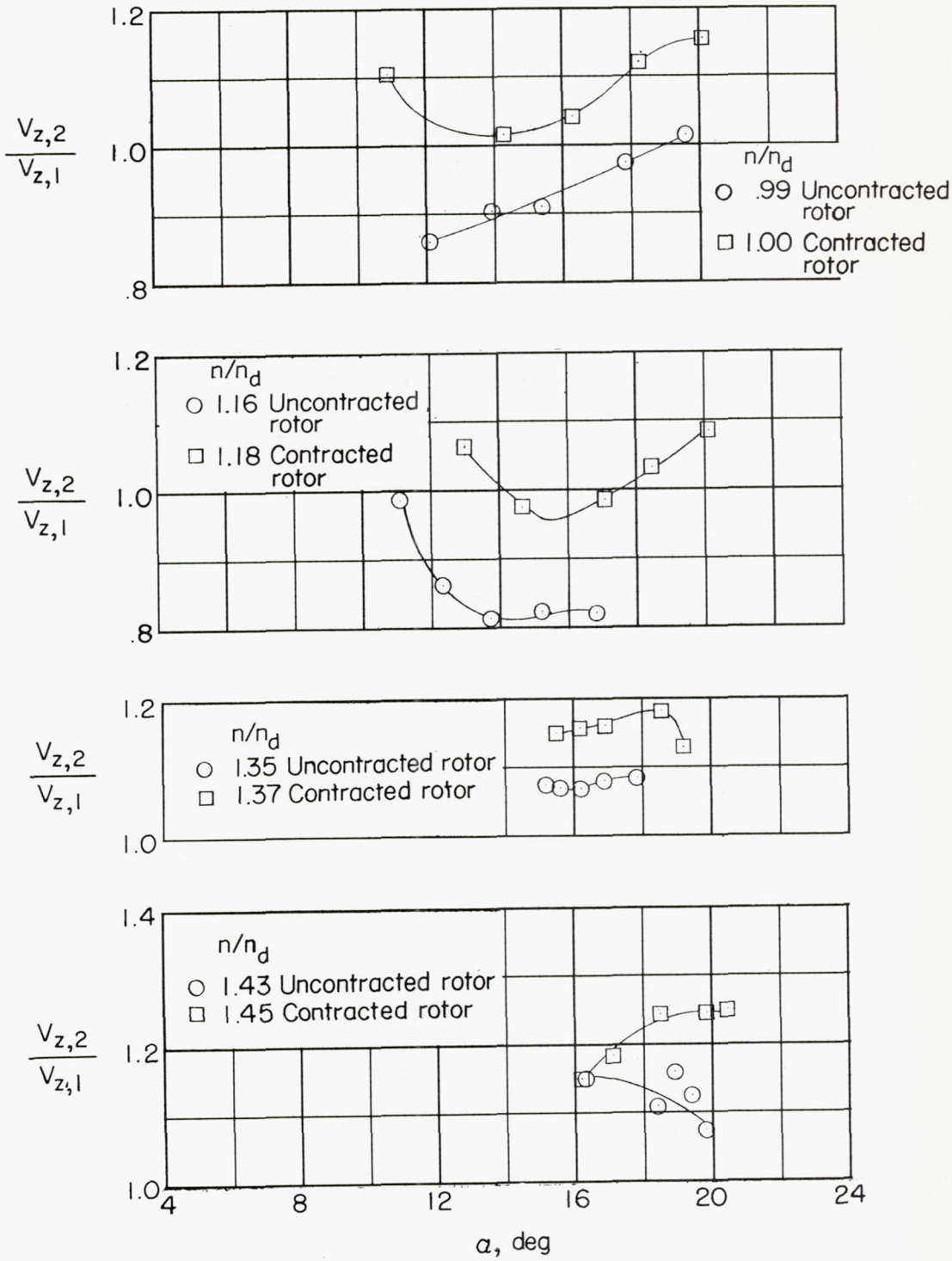

Figure 23.- Comparison of axial-velocity ratio at the hub section.

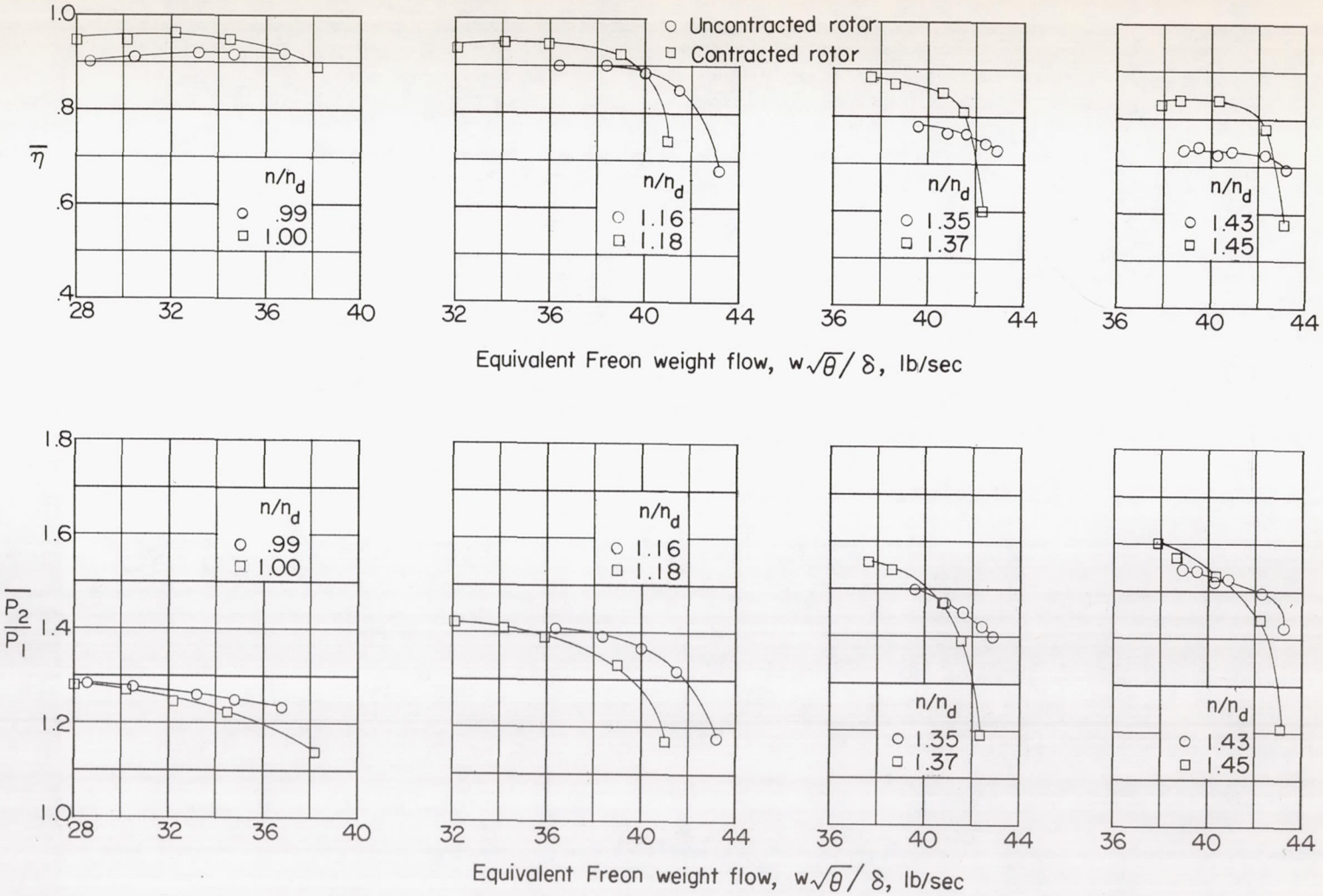

Figure 24.- Comparison plot of overall rotor performance.

NACA - Langley Field, Va.